Unsteady RANS Simulation of Turbulent Cavity Flow: Summary of 2D Baseline Computations

SHIA-HUI PENG

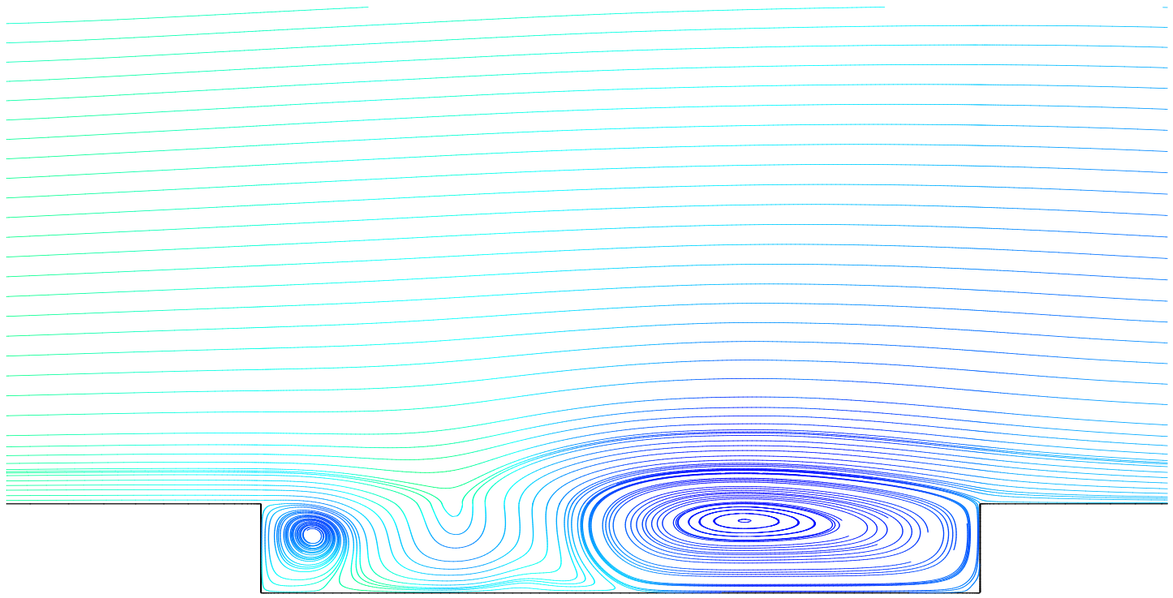

FOI
Swedish Defence Research Agency
SE-164 90 STOCKHOLM

Tel: +46 8 5550 3000
Fax: +46 8 5550 3100

www.foi.se

FOI-R--1915--SE
ISSN-1650-1942

Technical report
December 2005

Systems Technology

Shia-Hui Peng

Unsteady RANS Simulation of Turbulent Cavity Flow: Summary of 2D Baseline Computations

FOI-R--1915--SE Technical report **Systems Technology**
ISSN-1650-1942 December 2005

Issuing organisation FOI – Swedish Defence Research Agency Systems Technology SE-164 90 STOCKHOLM	**Report number, ISRN** FOI-R--1915--SE	**Report type** Technical report
	Research area code 7. Vehicles	
	Month year December 2005	**Project no.** E61109
	Sub area code 72. Air Vehicles	
	Sub area code 2 81. Unmanned Vehicles	
Author/s (editor/s) Shia-Hui Peng	**Project manager** Staffan Meijer	
	Approved by Monica Dahlén Head, Systems Technology	
	Sponsoring agency FMV	
	Scientifically and technically responsible Peter Eliasson	

Report title
Unsteady RANS Simulation of Turbulent Cavity Flow: Summary of 2D Baseline Computations

Abstract
A number of computations have been carried out for the flow over a rectangular open cavity that is similar to a weapon-bay geometry at a Mach number of $M_\infty = 0.85$. The calculations have been made for a 2D cavity configuration with an aspect ratio of 5 (a ratio between the cavity length and the cavity depth) using unsteady RANS (URANS) modelling. The simulation serves as baseline-type computations, with an effort to efficiently investigate some numerical issues encountered commonly in industrial CFD modelling for 2D cavity flows. As a result, it is expected that such an investigation may give some implications to 3D URANS and DES (detached eddy simulation) modelling based on a 3D cavity geometry. This memorandum summarizes the results of 2D URANS computations in analysis of wall-pressure fluctuations at the cavity floor in terms of the power spectral density (PSD) and sound pressure level (SPL). The results have been compared with available experimental measurements. The emphasis is placed on the effect of grid resolution with four different meshes. It is shown that the results are very sensitive to the grid resolution for the incoming boundary layer and for the shear layer over the cavity opening.

Keywords
Unsteady RANS, Cavity flow, Pressure fluctuations, Power spectral density (PSD), Sound pressure level (SPL), Mesh resolution

Further bibliographic information	**Language** English
ISSN ISSN-1650-1942	**Pages** 32 p.
	Price acc. to pricelist

Utgivare FOI – Totalförsvarets forskningsinstitut Systemteknik 164 90 STOCKHOLM	**Rapportnummer, ISRN** FOI-R--1915--SE	**Klassificering** Teknisk rapport
	Forskningsområde 7. Farkoster	
	Månad år December 2005	**Projektnummer** E61109
	Delområde 72. Luftfarkoster	
	Delområde 2 81. Obemannade farkoster	
Författare/redaktör Shia-Hui Peng	**Projektledare** Staffan Meijer	
	Godkänd av Monica Dahlén Chef, Systemteknik	
	Uppdragsgivare/kundbeteckning FMV	
	Tekniskt och/eller vetenskapligt ansvarig Peter Eliasson	

Rapportens titel
Instationär RANS-simuleringar av turbulent kavitetsströmning: sammanfattning av 2D *baseline* beräkningar

Sammanfattning

Ett antal beräkningar har genomförts för strömming över en rektangulär öppen kavitet som påminner om ett vapenschakt vid ett Machtal på M=0.85. Beräkningarna har gjorts för en 2D kavitet med ett sidoförhållande på 5 (förhållandet mellan kavitetens längd och djup) med instationär RANS (URANS). Undersökningar avseende nätupplösning har gjorts och det är tänkt att dessa resultat ska ligga som grund till ytterligare studier i 3D med URANS och DES. Denna rapport sammanfattar resultaten med 2D URANS genom att studera tryckfluktuationer på kavitetens nedre vägg i termer av effekttäthetsspektrum (power spectral density, PSD) och ljudtrycksnivå (sound pressure level, SPL). Resultaten har jämförts med experimentella data. Tyngdpunkten ligger på effekten av nätupplösning med fyra olika beräkningsnät. Resultaten visar på känslighet i nätupplösning för det inkommande gränsskiktet samt för skärskiktet över kaviteten.

Nyckelord
instationär RANS, kavitetsströmming, tryckfluktuationer, effekttäthetsspektrum (PSD), ljudtrycksnivå (SPL), nätupplösning

Övriga bibliografiska uppgifter	**Språk** Engelska
ISSN ISSN-1650-1942	**Antal sidor:** 32 s.
Distribution enligt missiv	**Pris: Enligt prislista**

Contents

1 Introduction

Unsteady flow over cavity geometries occurs in a variety of applications such as gate slots and aircraft components. The cavity flow belongs to a basic class of flows susceptible to self-sustaining oscillations. In industrial practice, the cavity-type oscillation is undesirable from the perspective of inducement of structure vibration and fatigue, generation of noise and drastic increase in drag on the body where the cavity is embedded. This type of flows has been extensively studied over the past 50 years since the pioneering work of Roshko [1], as reviewed recently by Colonius [2].

Many of previous studies have focused on the acoustical analysis generated by pressure oscillations in the cavity. Some cavities known as closed cavities may lead to broadband noise when immersed into a flow field. Provided that the length of the cavity is long enough compared to the incoming boundary layer thickness, nonetheless, the cavity flow is generally characterized by large pressure fluctuations at discrete frequencies [3]. The oscillation in the form of *wake mode*, as specified by Gharib and Roshko [4], for example, could trigger fluid-structure interactions, causing intense drag fluctuations due to the ejection of very large vortices out of the cavity. Such behavior seems to be preferentially related to two-dimensional or axisymmetrical configurations. According to Rowley et al [5], on the other hand, in many cases the pressure oscillation may also be due to the *shear mode*, which represents the coupling between the mixing layer over the cavity opening and the pressure field. The resonant frequencies for this coupling has often been analyzed by the Rossiter formula [6], viz.

$$f_n = \frac{U_\infty}{L}\frac{n-\gamma}{M_\infty + 1/\kappa}, \tag{1.1}$$

where U_∞ and M_∞ are the freestream velocity and Mach number, respectively, L is the length of the cavity, n is the mode number, γ and κ are two empirical constants.

Most cavity flows of practical interest are turbulent flows, which must be modelled to represent the effect of turbulence. Apart from other more advanced (and thus usually more expensive) modelling approaches, for example, detached eddy simulation (DES) and large eddy simulation (LES), which are emerging for cavity-flow simulations in recent years, Reynolds-Averaged Navier-Stokes (RANS) modelling approaches have long and commonly been used, see e.g. [7, 8, 9]. The RANS modelling of cavity flows is challenging in terms of flow physics and some numerical issues. As mentioned, cavity flows are usually unsteady due to self-sustained pressure oscillations, which requires thus time-dependent simulations. Unsteady RANS modelling has been generally employed in the literature, being applied to either 2D or 3D configurations, or to both. The chosen RANS model should be able to represent appropriately the incoming boundary layer and, particularly, to resolve correctly the subsequent shear layer and its instabilities, which is directly coupled with the oscillating pressure pattern in the cavity. Additionally, the model should also be able to represent unstationary flow recirculation and reattachment, vortical rolling and

breakdown occurring in the cavity and downstream. On the other hand, cavity flows are closely characterized by the geometric configuration. With a different aspect ratio, the cavity flow may become a rather different type with very different flow properties. This thus requires special attention paid to numerical specifications, for example, in terms of mesh resolution and time step, in order to reach a reasonable resolution of the flow unsteadiness and the unstationary flow properties.

In this memorandum, a number of 2D URANS computations are summarized for a subsonic flow past a $5:1$ rectangular cavity at a freestream Mach number of $M_\infty = 0.85$ with a Reynolds number as high as $Re = 7 \times 10^6$. The geometry has been employed to mimic a weapon bay during a store-release operation of an aircraft with cavities embedded in the aircraft fuselage. At the preliminary stage of the work, the simulation was performed for a 2D cavity configuration, which has been taken as the baseline computation in studies of some numerical and physical modelling issues. This is, consequently, expected to give some implications for further URANS and DES modelling based on a 3D cavity configuration, as will be reported separately. The computed results have been compared with available experimental data measured by QinetiQ [10, 11]. It should be noted that a part of the work summarized in this memorandum was initiated from a previous project TurMMAC, which was a collaborative project between the UK and Sweden. Some of the present results have been incorporated in the project final report [12]. The effort has been continued in the FOI FoT25 project "Utformning Lågsignaturfarkost", where more computations have been undertaken using refined grid resolutions, and a 3D URANS computation has been carried out. Recently, the modelling work for the 3D cavity flow has been further extended to the use of Detached Eddy Simulation (DES) as a test case in the EC project DESider.

2 Numerical Aspects

In this section, some numerical aspects are briefly described. These include the CFD solver, EURANUS, and the related numerical setup employed in the computations. Four structured grids have been used with different resolutions for the same cavity geometry under the flow conditions same as those used in the wind-tunnel experiment.

2.1 The CFD solver

All the simulations have been carried out using the structured Navier-Stokes solver EURANUS [13], which is a multi-purpose CFD code originally developed for handling compressible aerodynamic flows on structured multiblock meshes. Detailed description can be found in Ref. [14]. Only are some aspects related to the present computations briefly summarized here.

The EURANUS code solves the Navier-Stokes equations based on the finite volume method. For turbulent flows, the Reynolds-averaged equation system is closed using a number of different turbulence modelling closures, including algebraic zero-equation RANS models, two-equation RANS models, algebraic Reynolds stress models and DES models. The code employs an explicit, multistage Runge-Kutta scheme in conjunction with multigrid acceleration and implicit/explicit residual smoothing. For unsteady flow computations, the calculation can be advanced in time using either explicit Runge-Kutta time marching with a global time step or a second-order implicit temporal scheme with explicit subiterations. The latter is known as the dual-time stepping approach, where a global physical time step is employed and the local time step (the pseudo time) is used in the explicit subiterations.

The discretization in space is based on a cell-centered control volume method. The viscous fluxes are estimated using the second-order central scheme. The inviscid fluxes discretized from the convection terms can either use the second-order central scheme or use the first- or second-order upwind scheme.

The results presented here have been computed using the Spalart-Allmaras (S-A) turbulence model [15]. The implicit second-order time advancement has been employed by means of the dual-time stepping method, in which a five-stage Runge-Kutta scheme has been incorporated for the explicit subiterations. The second-order central scheme has been used for the momentum equations and the second-order upwind scheme for the turbulence transport equation. Note that, with the central scheme, an explicit artificial dissipation has been added for numerical stability. In addition, all the meshes employed in the computations have been generated in such a way that multi-level grids can be produced for the use of the FAS-based multigrid approach, where the W-cycle has been chosen in all the computations.

2.2 The computational set up

In the experiment conducted by QinetiQ, the open cavity (termed *M219 cavity*) is contained in a flat plate with a length of 72 inches and 17 inches in width, which is mounted in a transonic wind tunnel [16]. The M219 test case includes two configurations for the cavity embedded in the flat plate. The two configurations differ only in that one was tested with bay doors open at 90 degrees and the other with bay doors removed. The former is more two-dimensional in feature due to the blocking of spanwise flow entrainment by the doors [12]. The measurement with this configuration (i.e. the *door-on* case) has thus been used in comparison with the present 2D computations.

The rectangular empty cavity has dimensions of $L = 20$ inches in length, $D = 4$ inches in depth and $W = 4$ inches in width, giving a ratio of $L : D : W = 5 : 1 : 1$, see Figure 2.1. The experiment was performed under freestream conditions of $M_\infty = 0.85$, $P_\infty = 6.21 \times 10^4 Pa$, $T_\infty = 266.53K$ and $Re = 13.47 \times 10^6$ per meter.

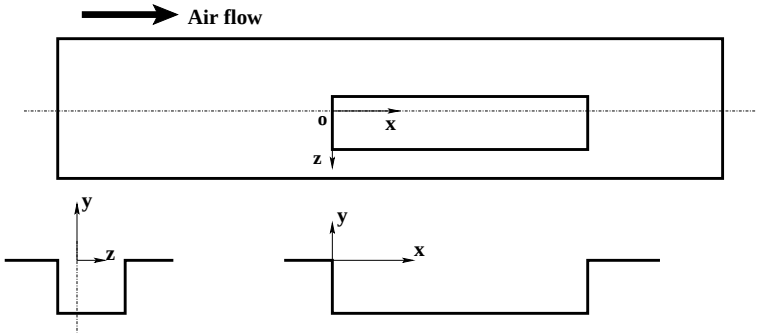

Figure 2.1: The sketch of the cavity geometry embedded in a 72 inches $\times$17 inches flat plate.

The time histories of wall-surface pressures for the door-on case were measured at a frequency of 6 kHz at a number of locations including 10 equally spaced points at positions along the cavity floor. Table 2.1 gives the positions of the kulite pressure measurement at the cavity floor (k20-k29) and at the rear wall (k17-k18).

Location	Kulite	x (inches)	z (inches)	y (inches)
Rear wall	k17	20.0	2.75	-0.75
	k18	20.0	2.75	-1.5
Floor	k20	1.0	0.0	-4.0
	k21	3.0	0.0	-4.0
	k22	5.0	0.0	-4.0
	k23	7.0	0.0	-4.0
	k24	9.0	0.0	-4.0
	k25	11.0	0.0	-4.0
	k26	13.0	0.0	-4.0
	k27	15.0	0.0	-4.0
	k28	17.0	0.0	-4.0
	k29	19.0	0.0	-4.0

Table 2.1: Kulite transducer positions along the cavity floor and at the rear wall for pressure measurements.

The computational domain, shown in Figure 2.2, is specified with dimensions of $L_x \times L_y$ in the $x-$ and $y-$directions, respectively. Four different grids have been used in the simulation, as summarized in Table 2.2. Two different computational domains have been employed, which have various sizes in the $y-$direction (with different L_y). The domain size in the $x-$direction is the same, however, having $L_x = 18D$. The upstream distance from the leading edge of the flat plate to the front wall (at $x = 0$) of the cavity is $7.75D$. The downstream distance from the cavity back wall (at $x = 5D$) to the trailing edge of the plate is $5.25D$.

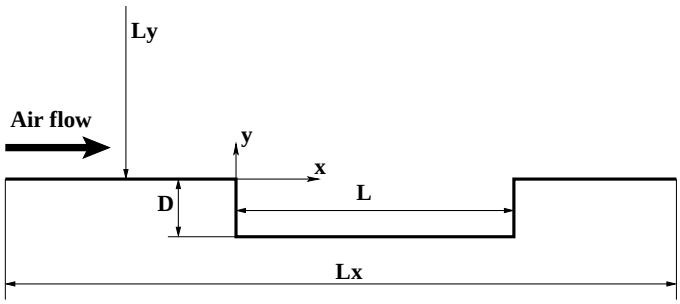

Figure 2.2: The sketch of the computational configuration.

Over all the wall surfaces, adiabatic wall boundary condition has been imposed. A symmetric boundary condition is assumed on the top boundary (at $y = L_y$). Two types of boundary conditions have been tested at both the upstream inflow section and the downstream outflow section. These include, respectively, the freestream boundary condition and the Riemann boundary condition. With the present computational domain, there is no obvious difference observed. The results presented below have been computed using the Riemann boundary condition at both the inflow and outflow sections.

The Spalart-Allmaras model has been used in all the computations presented in this memorandum. Nonetheless, a preliminary test has also been performed using the standard $k - \omega$ model by Wilcox [17] on the coarse mesh (C-mesh, see table 2.2). It was found that this model may dampen the unsteadiness and eventually drive the flow being steady due to an overestimated eddy viscosity. For comparison of the results obtained with different meshes, only the result obtained with the S-A model has been included.

Mesh	C-mesh	M-mesh	NM-mesh	F-mesh
Domain, $L_x \times L_y$	$18D \times 17D$	$18D \times 17D$	$18D \times 7.5D$	$18D \times 7.5D$
Node number	19884	33036	20930	51410
Cells in cavity	120×64	200×80	128×64	176×96
Cells above cavity	200×56	280×56	192×64	352×96
Time step, Δt	$0.01095T_0$	$0.01095T_0$	$0.01095T_0$	$0.00822T_0$

Table 2.2: Mesh resolution and time steps used in the computation, where $T_0 = L/U_\infty$.

Four groups of structured meshes with different resolutions and multiple blocks have been involved in the computations, as summarized in Table 2.2. These include a coarse mesh (C-mesh), a medium mesh (M-Mesh) and a fine mesh (F-mesh). In addition, a non-matching coarse mesh (NM-mesh) is also included. Note that the number of nodes with the NM mesh is comparable with that of the C-mesh, but the domain size L_y is reduced. The same reduced

domain is also adopted for the F-mesh. The NM-mesh divides the domain into two blocks. The first block contains only the cavity and the other accounts for the part above the cavity. The two blocks have a common connecting boundary over the cavity opening, where the nodes from both blocks are not matched with each other. From the M-mesh to the F-Mesh, the number of nodes in the cavity is not significantly increased, but rearranged for a better resolution for the shear layer over the cavity opening. Both the NM-mesh and F-mesh have been made to refine the resolution for the incoming upstream boundary layer, as well as for the shear layer.

3 Summary of Results

The results computed with the four different meshes are summarized in this section. The emphasis in the presentation is placed on the analysis of the predicted pressure fluctuations of which the time history, $P(t)$, has been recorded at positions along the cavity floor and on the cavity rear wall. The pressure oscillation is closely related to the sound resonance from the cavity. The recorded $P(t)$ has thus been used to compute the power spectral density (PSD) and the sound pressure level (SPL) as functions of frequency, respectively. The PSD describes how the power of the $P(t)$ is distributed with the frequency. It is computed from a Fourier transform of the autocorrelation of $P(t)$. From the convolution theorem, it can be defined as the squared modulus of Fourier transform of $P(t)$. In this work, the discrete Fourier transform has been used to compute the PSD.

The sound pressure level (SPL) is related to PSD as a function of frequency, which is defined by

$$SPL = 10 \log \left(\frac{PSD}{p_{ref}^2} \right), \tag{3.1}$$

where $p_{ref} = 2 \times 10^{-5}$ Pa is the value adopted as the minimum audible sound pressure variation.

The mean pressure is obtained by time-averaging the pressure history, viz.

$$\overline{P} = \frac{1}{N - N_0} \sum_{k=N_0}^{N} P_k(t), \tag{3.2}$$

where N is the total sampling number of the time series, N_0 is the sampling number with which the time-averaging starts. The root mean square of the pressure fluctuations can then readily be computed from

$$P_{rms} = \frac{1}{N - N_0} \sum_{k=N_0}^{N} \left(P_k(t) - \overline{P} \right)^2. \tag{3.3}$$

With the root mean square of the pressure, P_{rms}, the time-averaged sound pressure level, $\overline{SPL}$ may also be used in practice, which is defined by

$$\overline{SPL} = 20 \log \left(\frac{P_{rms}}{p_{ref}} \right). \tag{3.4}$$

Note that the time-averaged sound pressure level, $\overline{SPL}$, has sometimes been termed *pressure intensity* in the literature.

It should be noted that, upon the initial flow field with which the unsteady computation starts, it takes usually a certain time period, t_0, until the simulated flow has been fully developed. This can be justified in unsteady computations by an observation of the recorded transient quantities at a probed position, which should fluctuate with time around a constant mean value after t_0. In the analysis of $P(t)$, therefore, an initial time period of $t_0 = (10 \sim 50)T_0$ has usually been discarded.

3.1 Results computed with different meshes

Based on the experimental data, there are four Rossiter modes observed with frequencies approximately at $f_1 = 180Hz$, $f_2 = 390Hz$, $f_3 = 590Hz$ and $f_4 = 820Hz$, respectively. The second mode at $f_2 = 390Hz$ is the dominant one with the largest magnitude in PSD and SPL. Applying the Rossiter formulation, Eq. (1.1), to these frequencies, it is found that one can take, for the two empirical coefficients, $\gamma = 0.14$ and $\kappa = 0.57$. Note that κ has usually been justified as a function of the freestrem Mach number, while γ is related to the aspect ratio of the cavity (L/D). In addition, for the door-on case (used for comparison with present 2D computations), the experiment has measured both the pressure fluctuation and the PSD at positions on the cavity floor and rear wall. It has been noted that, at several positions, the PSD computed from the measured $P(t)$ does not agree with the PSD measured directly in terms of the magnitude, but the frequency to each of the four tonal modes matches correctly. The comparison made below for PSD and SPL has been based on the measured PSD. In what follows, we present the results computed with different mesh resolutions and make a comparison with the experimental data.

3.1.1 Results with coarse mesh (C-mesh)

The illustration of the coarse mesh (C-mesh) is given in Figure 3.1. The mesh is clustered near the wall surface. Over the horizontal walls, the first near-wall node is located generally at $y_1^+ = 2 \sim 3.5$, and near the cavity rear wall $x_1^+ \approx 5$. The mesh is rather stretched in both the $x-$ and $y-$directions.

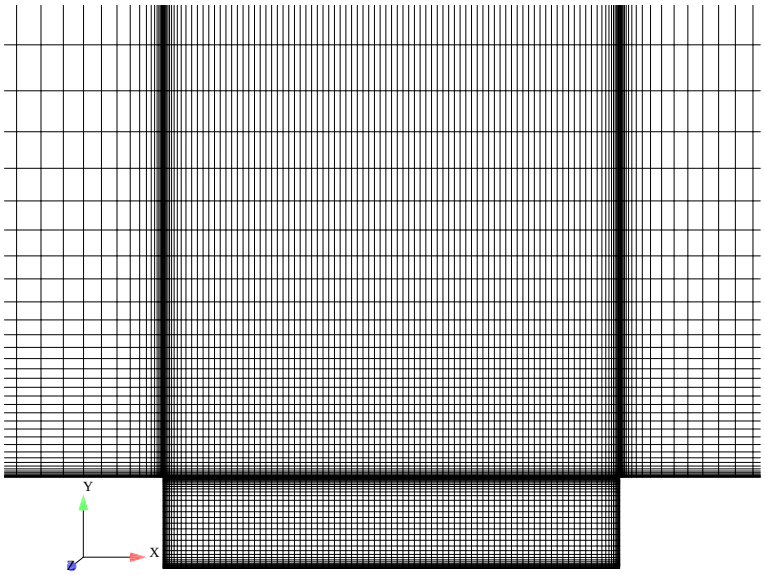

Figure 3.1: Illustration of the coarse mesh (C-mesh).

In Figure 3.2, the computed PSD and SPL are compared with the experimental measurements at positions k20, k22, k24, k25, k27 and k29, respectively, on the cavity floor. It is shown that the magnitude of both PSD and SPL is over-estimated at all the side positions on the cavity floor (k20 k22, k27 and k29), but the prediction is better for the mid-positions at k24 and k25. The prediction contains much less amount of broadband noise than the measured

PSD and SPL, but with additional tonal modes. This suggests that erroneous characteristic pressure patterns or mode shapes have been produced in the simulation. Nonetheless, Tracy et al. [18] reported similar modal distributions in their measurements for cavity flows at $M_\infty = 0.8$ and 0.9 with $L/D = 4.4$ and 6.70, respectively, which are similar to the flow conditions used in the present computation.

In Figure 3.3, the computed PSD and SPL are presented for postions k17 and k18 at the cavity rear wall (located at $x = L$). As shown, the predicted magnitudes at k17 and k18 are in better agreement with the measured data than those computed at the cavity floor. Of all the positions along the floor and on the rear wall, the frequency of the second mode measured experimentally at $f_2 \approx 390Hz$ corresponds approximately to the third mode frequency in the prediction. The frequency for the first mode has been predicted at a lower value than the measured one.

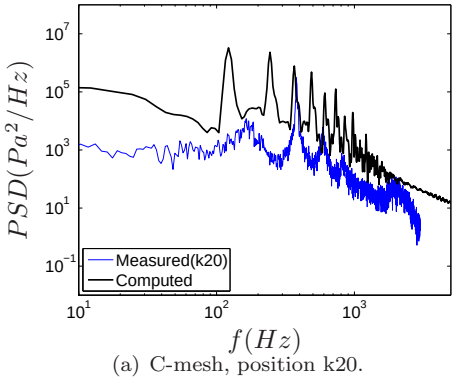

(a) C-mesh, position k20.

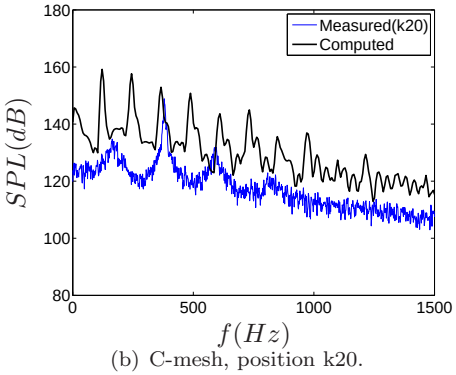

(b) C-mesh, position k20.

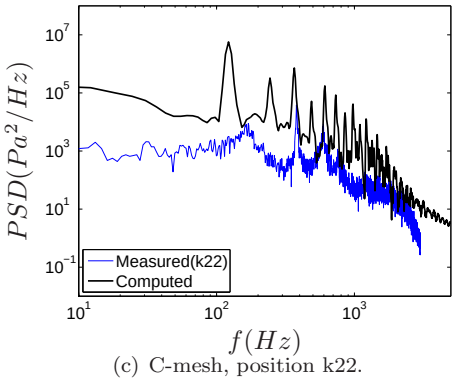

(c) C-mesh, position k22.

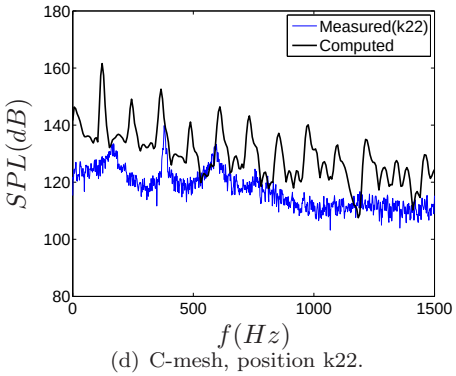

(d) C-mesh, position k22.

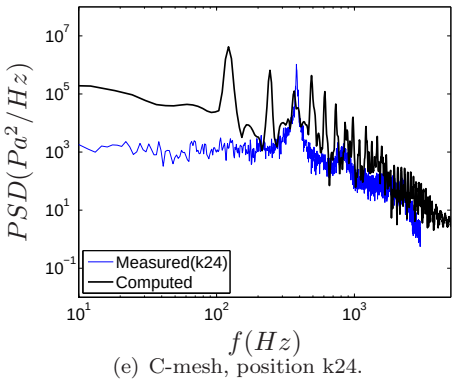

(e) C-mesh, position k24.

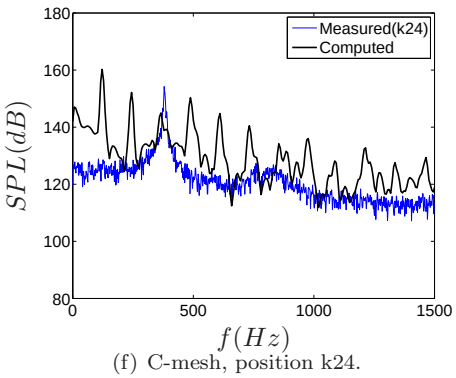

(f) C-mesh, position k24.

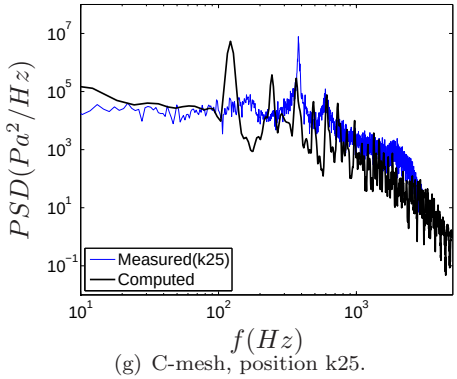

(g) C-mesh, position k25.

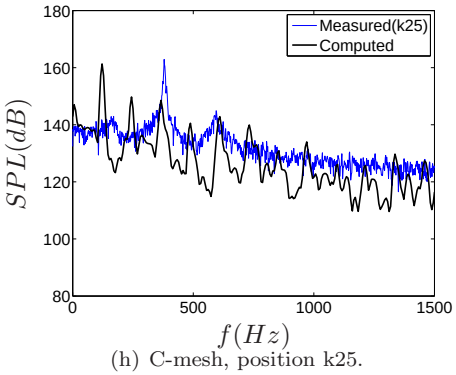

(h) C-mesh, position k25.

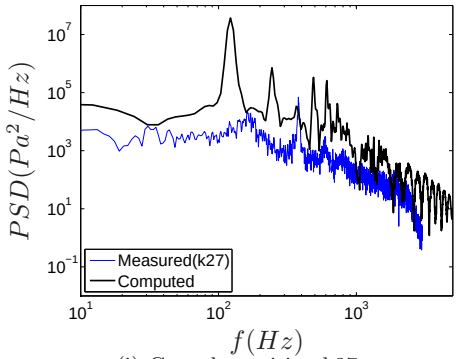

(i) C-mesh, position k27.

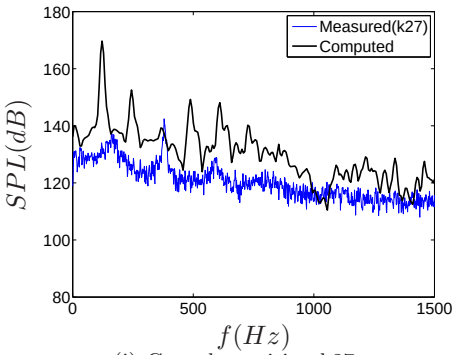

(j) C-mesh, position k27.

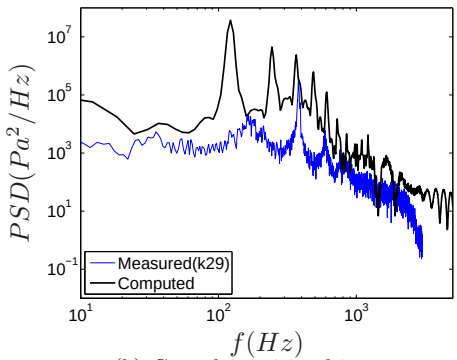

(k) C-mesh, position k29.

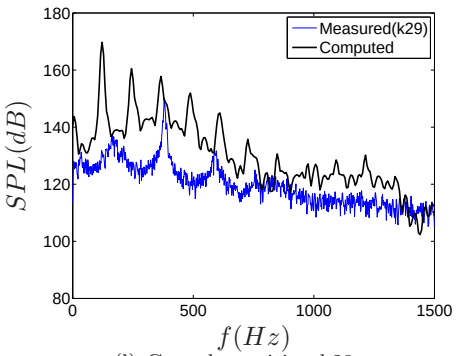

(l) C-mesh, position k29.

Figure 3.2: C-mesh: computed PSD of pressure fluctuations and SPL at positions k20, k22, k24, k25, k27 and k29 on the surface of the cavity floor.

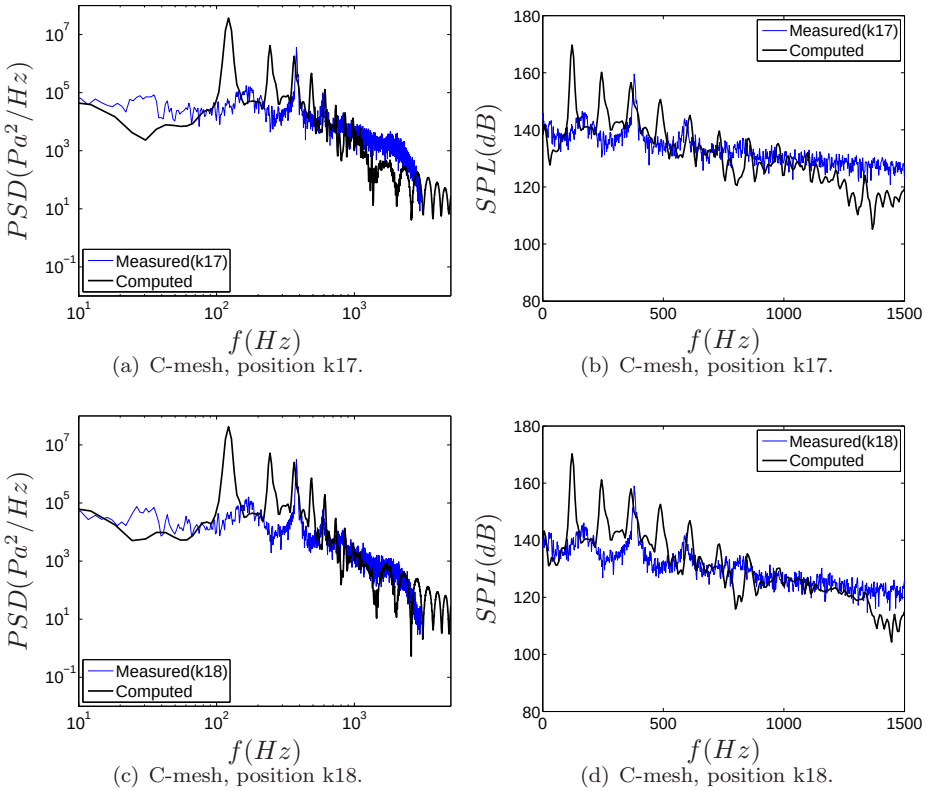

(a) C-mesh, position k17. (b) C-mesh, position k17.

(c) C-mesh, position k18. (d) C-mesh, position k18.

Figure 3.3: C-mesh: computed PSD of pressure fluctuations and SPL at positions k17 and k18 on the rear-wall surface of the cavity.

3.1.2 Results with medium mesh (M-Mesh)

The medium mesh (M-mesh) is illustrated in Figure 3.4, which has the same computational domain as the C-mesh. The M-mesh is refined in the cavity in both the $x-$ and $y-$direction, but is only refined in the $x-$direction over the block above the cavity, as given in Table 2.2. The near-wall resolution is the same as with the C-mesh, giving generally $y_1^+ = 2 \sim 3.5$, and $x_1^+ \approx 5$ near the cavity rear wall.

A comparison is made in Figure 3.5 between the prediction and the experimental measurement for PSD and SPL, respectively, at positions along the cavity floor. The grid refinement has indeed significantly reduced the predicted magnitudes for both PSD and SPL, and has brought the predictions somewhat closer to the experiment than those obtained with the C-mesh for positions along the floor from the front wall to the middle of the cavity (namely at positions k20-k25). At positions k27 and k29 towards the rear wall of the cavity, the magnitude of PSD and SPL is still over-predicted. The tonal mode exhibits a broader bound than that arising from the C-mesh prediction, and the tonal peak becomes less distinguishable except for that of the first mode.

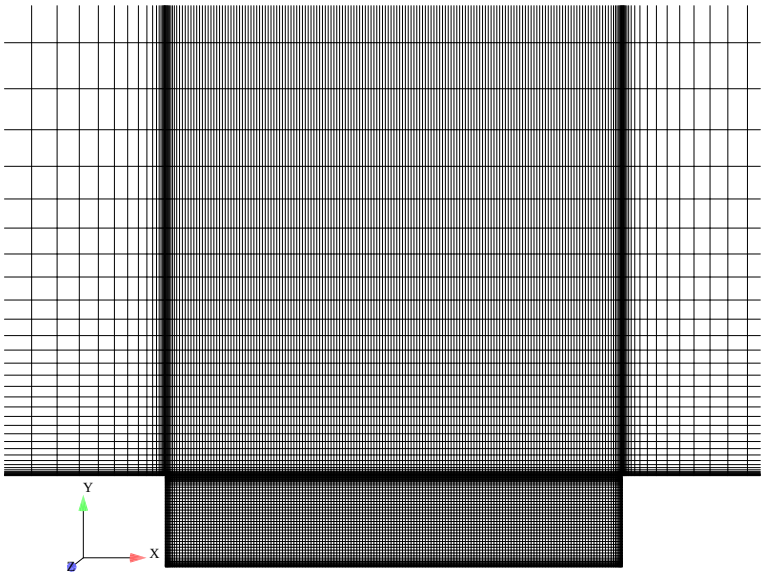

Figure 3.4: Illustration of the medium mesh (M-mesh).

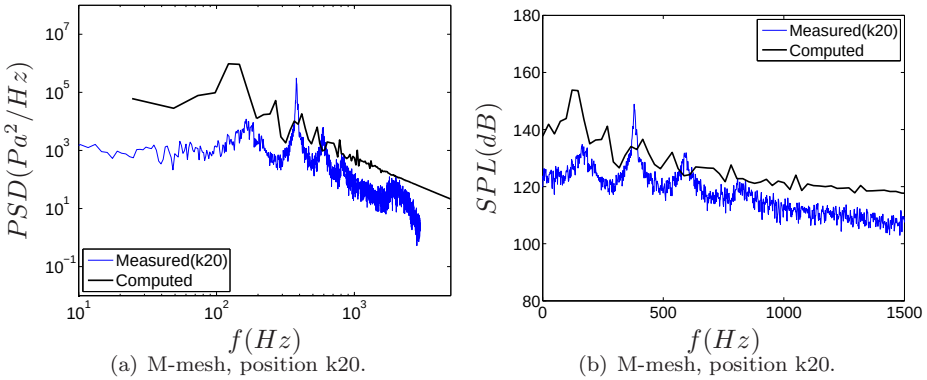

(a) M-mesh, position k20.

(b) M-mesh, position k20.

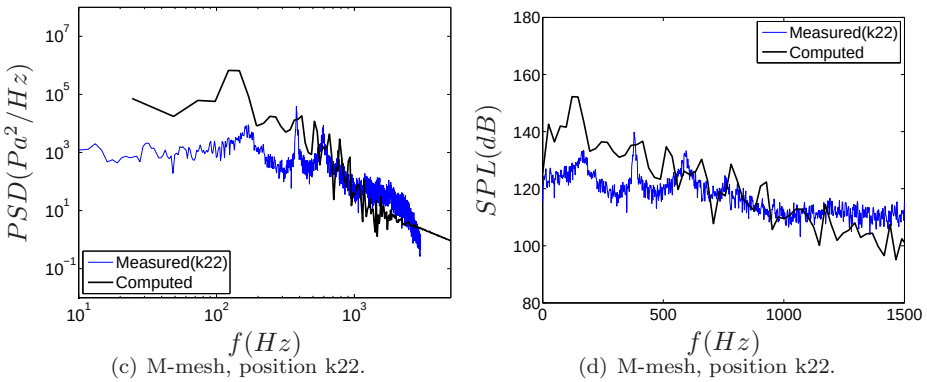

(c) M-mesh, position k22.

(d) M-mesh, position k22.

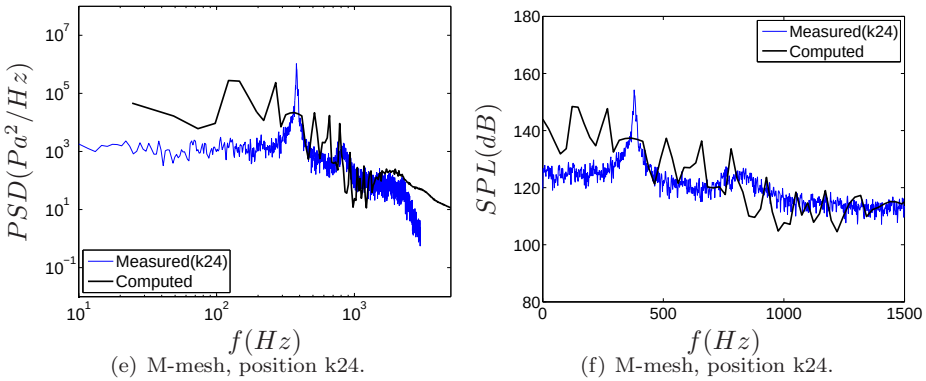

(e) M-mesh, position k24.

(f) M-mesh, position k24.

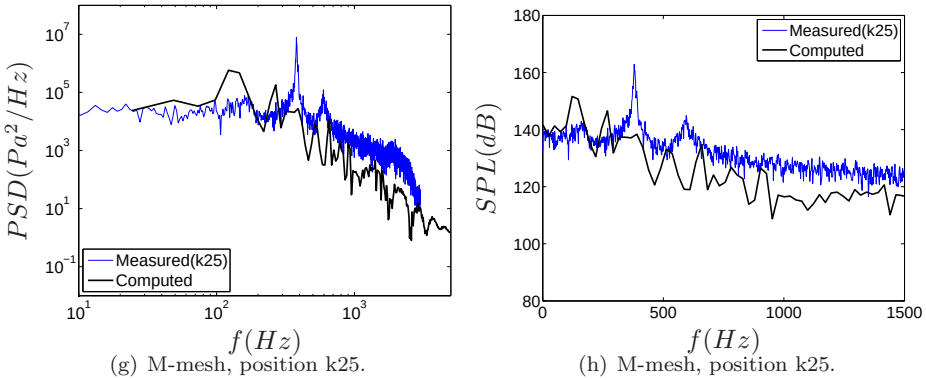

(g) M-mesh, position k25.

(h) M-mesh, position k25.

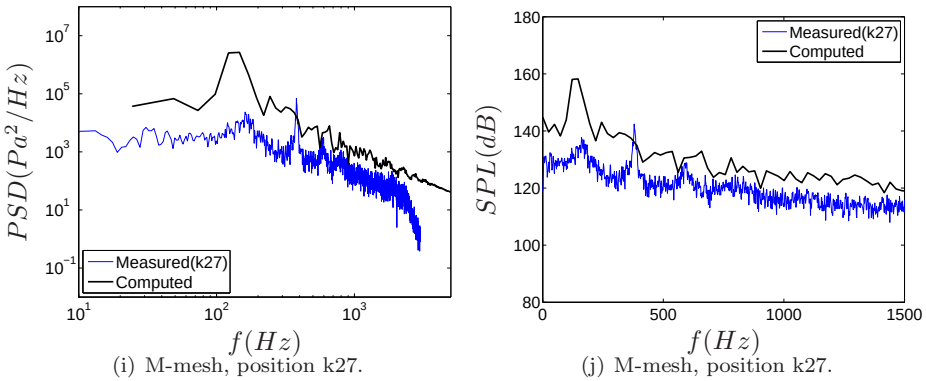

(i) M-mesh, position k27.

(j) M-mesh, position k27.

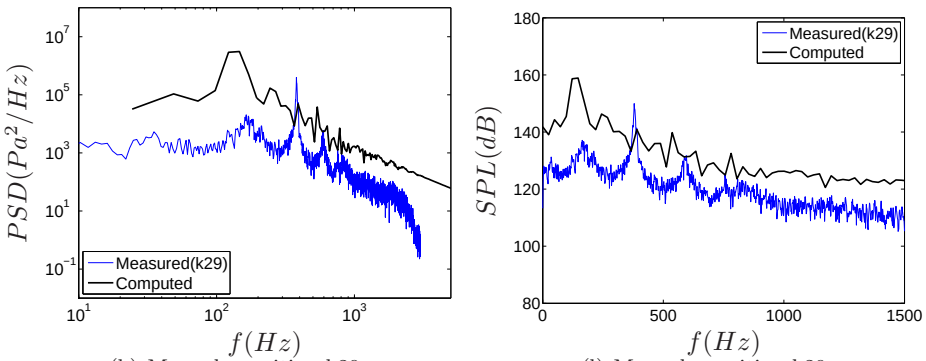

(k) M-mesh, position k29.

(l) M-mesh, position k29.

Figure 3.5: M-mesh: computed PSD of pressure fluctuations and SPL at positions k20, k22, k24, k25, k27 and k29 on the surface of cavity floor.

At the postions on the cavity real walls, k17 and k18, as shown in Figure 3.6, the predicted PSD and SPL are roughly comparable with the experimental data at high frequencies. For the first mode, the magnitude is over-predicted and corresponds to a frequency lower than the measured $f_1 = 180Hz$, while for the other modes, the tonal peaks have become less sensible than that obtained from the C-mesh prediction.

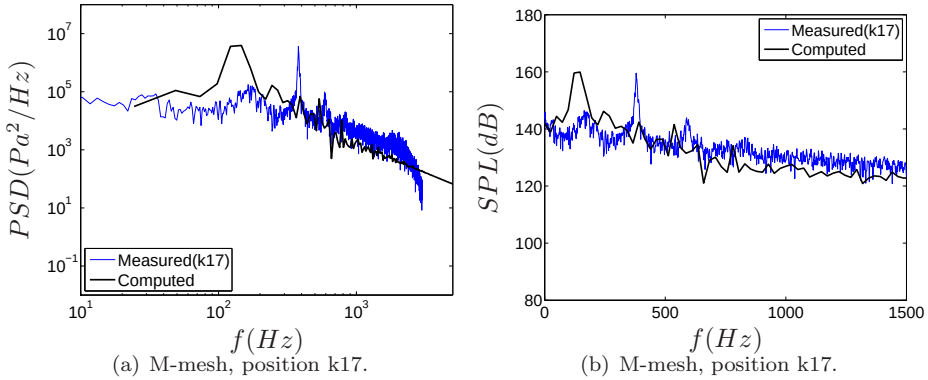

(a) M-mesh, position k17.

(b) M-mesh, position k17.

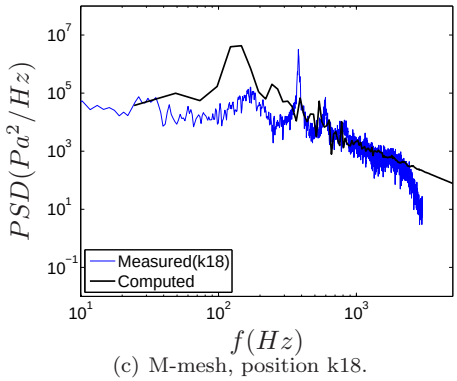

(c) M-mesh, position k18.

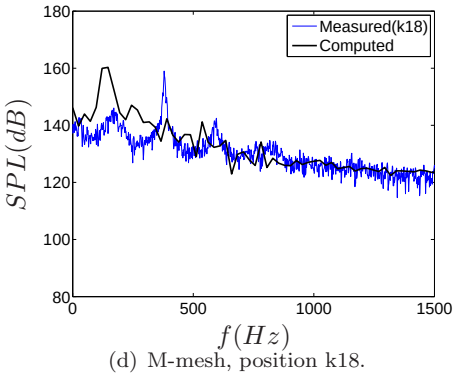

(d) M-mesh, position k18.

Figure 3.6: M-Mesh: computed PSD of pressure fluctuations and SPL at positions k17 and k18 on the rear-wall surface of the cavity.

3.1.3 Results with non-matching mesh (NM-Mesh)

The non-matching mesh (NM-mesh) is illustrated in Figure 3.7, where a close view is also given on the meshing over the cavity opening. The total node number and the node number in the cavity are similar to those with the C-mesh (see Table 2.2). The near-wall grid resolution is also similar to both the C-mesh and the M-mesh with $y_1^+ = 2 \sim 5$, and near the cavity rear wall $x_1^+ \approx 5.5$. The main difference, as compared with the C-mesh and M-mesh, is that the computational domain has reduced in the vertical $y-$direction. This has enabled a refined resolution in the block above the cavity with 64 cells in the vertical direction ($L_y = 7.5D$), whereas 56 cells are allocated with the C-mesh and M-mesh with $L_y = 17D$. In addition, the mesh is less stretched and the vertical grid resolution cross the cavity opening is about 2.6 times denser than the resolution in the C-mesh and M-mesh. One of the purposes with the NM-mesh is to observe the effect of the grid resolution in the shear layer over the cavity opening.

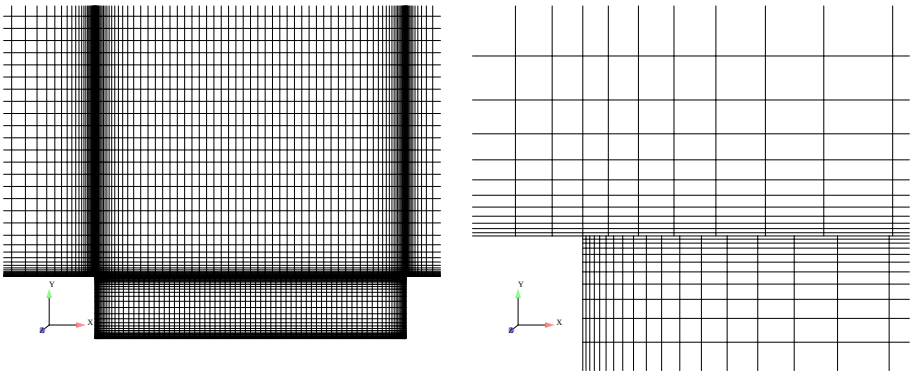

(a) The NM-mesh. (b) Close view of non-matching boundary.

Figure 3.7: Illustration of the non-matching mesh (NM-mesh).

Figure 3.8 gives the predicted PSD and SPL at postions along the cavity floor. The agreement between the predicted and measured magnitudes of PSD and SPL is improved at positions near the cavity front wall (k20 and k21) and near the rear wall (k28 and k29), as compared with the results at the same positions computed with the C-mesh and M-mesh, respectively. Nonetheless, at positions located in the mid-section of the cavity floor (k23-k26), the magnitudes are in general under-estimated, in contrast to the better predictions with the C-mesh and M-mesh. Moreover, with the NM-mesh, the first tonal mode has been identified in the prediction at $f_1 \approx 164Hz$ corresponding to the measured $180Hz$ and with a generally over-predicted magnitude. Considering that both the C-mesh and M-mesh predictions have produced a much lower frequency for the first mode, the improvement made with the NM-mesh prediction may imply that this mode has more to do with the resolution of the shear layer over the cavity opening.

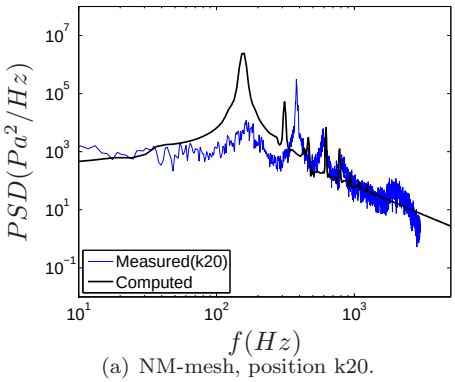

(a) NM-mesh, position k20.

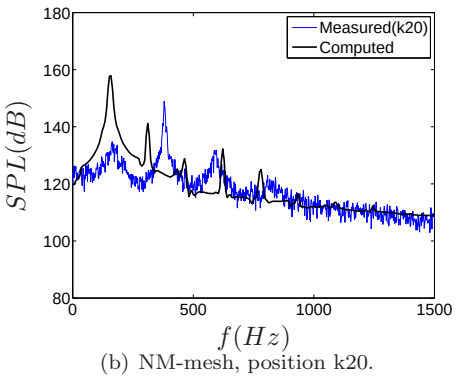

(b) NM-mesh, position k20.

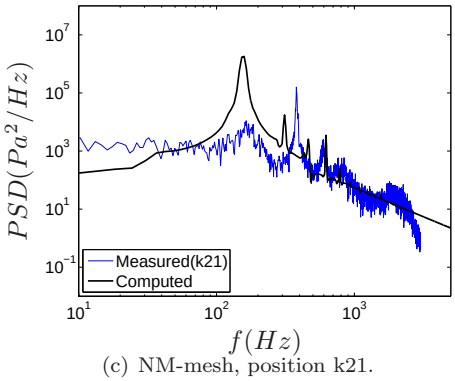

(c) NM-mesh, position k21.

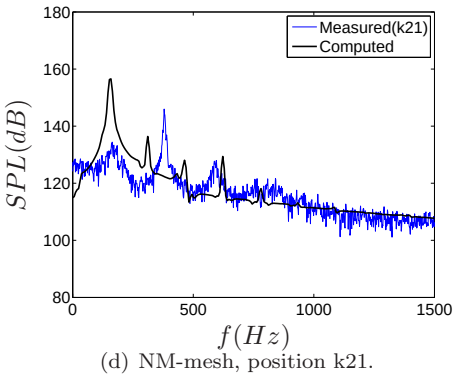

(d) NM-mesh, position k21.

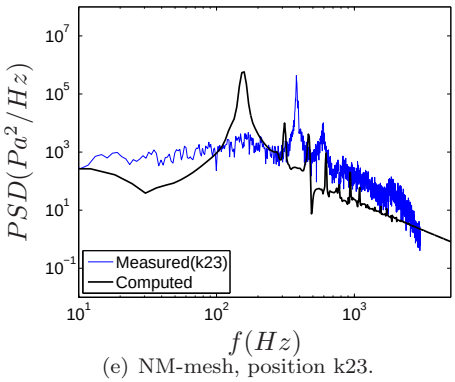

(e) NM-mesh, position k23.

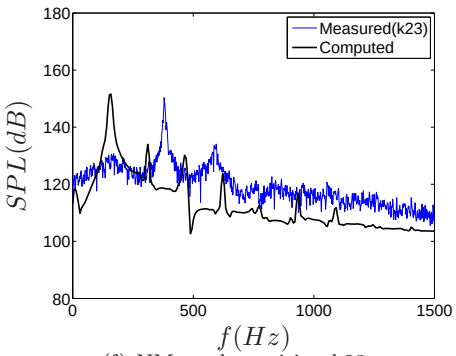

(f) NM-mesh, position k23.

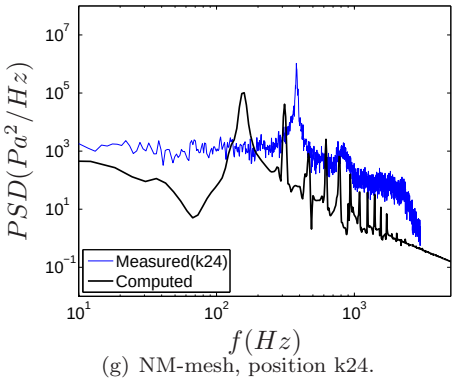

(g) NM-mesh, position k24.

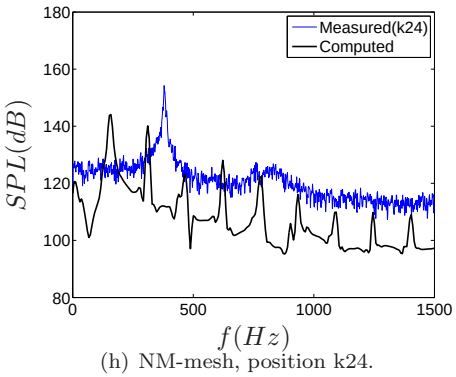

(h) NM-mesh, position k24.

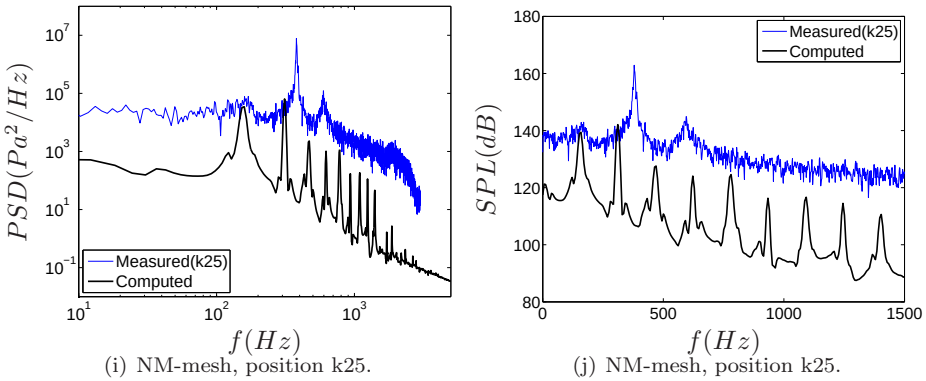

(i) NM-mesh, position k25.

(j) NM-mesh, position k25.

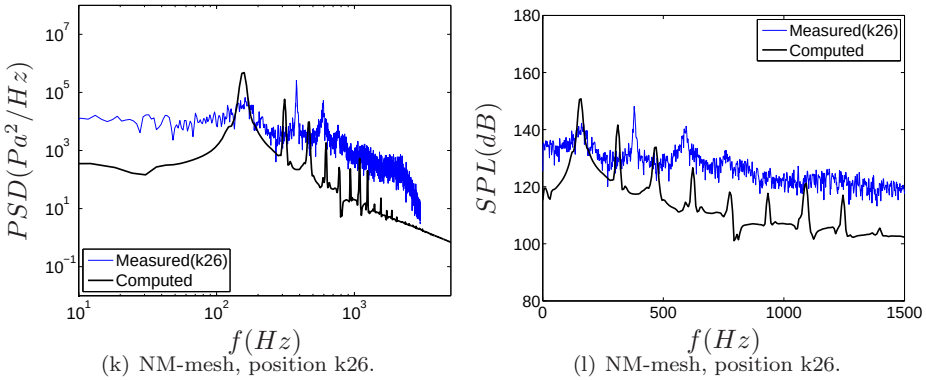

(k) NM-mesh, position k26.

(l) NM-mesh, position k26.

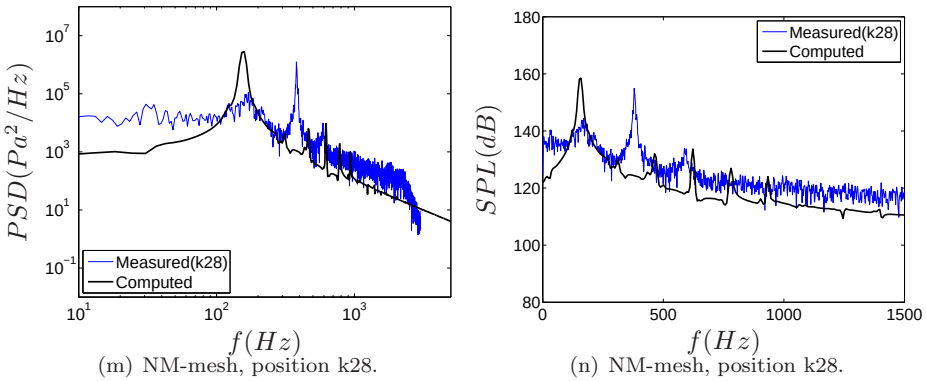

(m) NM-mesh, position k28.

(n) NM-mesh, position k28.

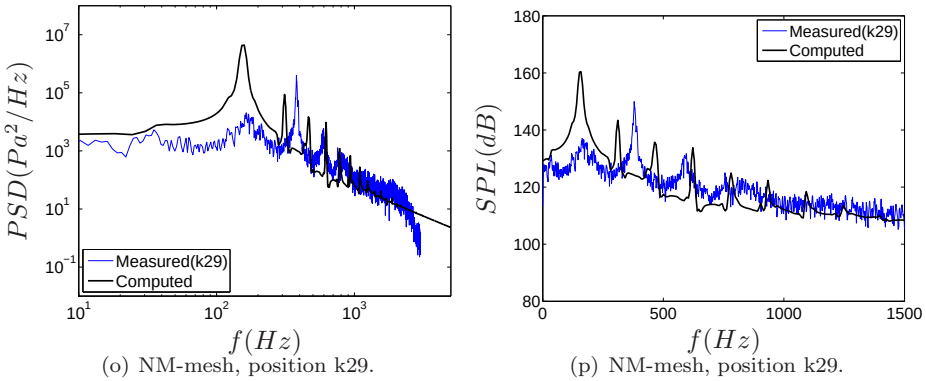

(o) NM-mesh, position k29.

(p) NM-mesh, position k29.

Figure 3.8: NM-mesh: computed PSD of pressure fluctuations and SPL at positions k20, k21, k23, k24, k25, k26 k28 and k29 on the surface of cavity floor.

In Figure 3.9, the prediction at position k17 on the cavity rear wall is presented. It is shown that the magnitude of PSD and SPL is generally underestimated, while the first tonal magnitude is over-predicted, although the frequency of this mode is captured better than the C-mesh and M-mesh predictions. Similar to the prediction with the C-mesh, additional unphysical modes are observed in the NM-mesh prediction.

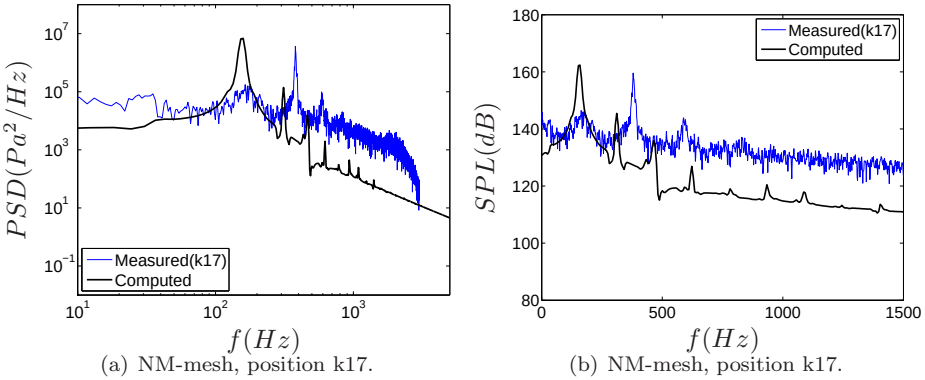

(a) NM-mesh, position k17. (b) NM-mesh, position k17.

Figure 3.9: NM-Mesh: computed PSD of pressure fluctuations and SPL at position k17 on the rear-wall surface of the cavity.

3.1.4 Results with fine mesh (F-Mesh)

Figure 3.10 illustrates the fine mesh (F-mesh), which employs a reduced computational domain in the vertical direction same as with the NM-mesh. An overall grid refinement has been made, particularly in the block above the cavity, with an effort to better resolve the incoming boundary layer and the subsequent shear layer. The resolution near the cavity floor is $y_1^+ \approx 1$, and $x_1^+ \approx 4$ near the cavity rear wall. Over the flat plate in the upstream and downstream boundary layers, the first node is generally located at $y_1^+ \approx 2.5 \sim 3.5$. The F-mesh has been refined in both the streamwise and vertical directions. The mesh is less stretched with a more uniform cell aspect ratio, being gridded in regions away from the wall surface. Furthermore, it should be noted that the time step used in the F-mesh simulation has been reduced (see Table 2.2) for the refined mesh in order to maintain numerical stability with an appropriate local CFL number.

The predicted PSD and SPL are compared with the measured data in Figure 3.11. It is shown that some improved predictions have been produced on the side locations of the cavity floor away from the mid-position (k24 and k25) toward the front wall and to the rear wall, respectively. The first tonal mode at $f_1 \approx 180Hz$ is reproduced at all locations along the cavity floor but with an over-estimated magnitude for both the PSD and SPL. The second mode, identified in the experiment at $f_2 \approx 390Hz$, shows a weak sign in the prediction at a somewhat larger frequency. A weak tendency with a diminished peak is also reproduced in the prediction for the third tonal mode as identified experimentally at $f_3 \approx 590Hz$. Both the predicted second and third mode presents somewhat larger frequencies than the experimentally measured $390Hz$ and $590Hz$, respectively, with tonal magnitudes underestimated obviously.

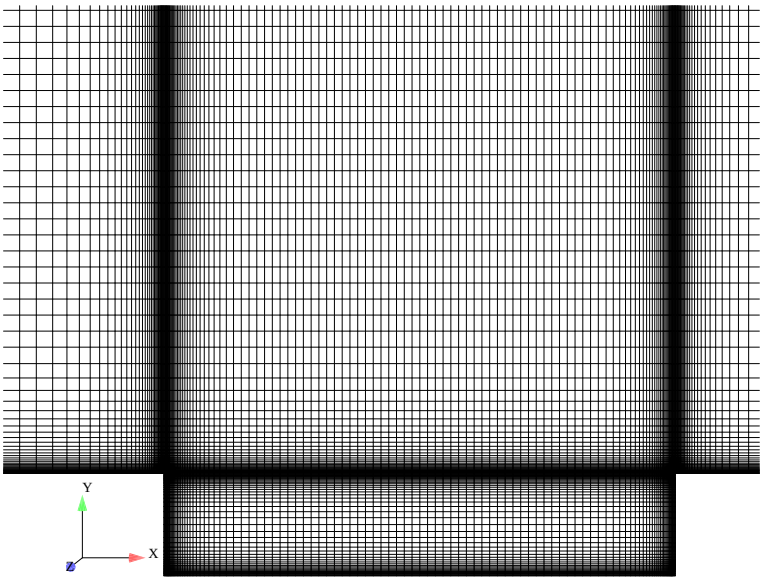

Figure 3.10: Illustration of the fine mesh (F-mesh).

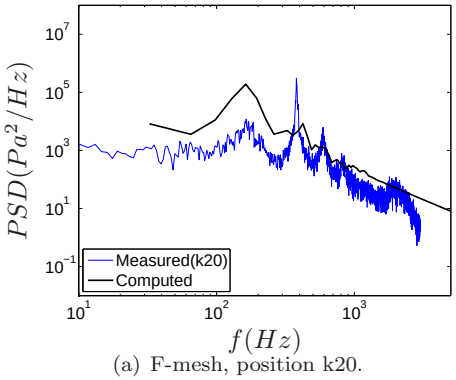

(a) F-mesh, position k20.

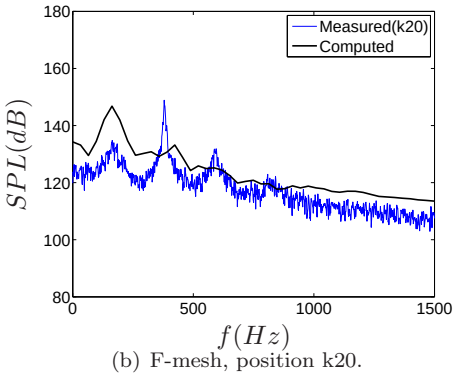

(b) F-mesh, position k20.

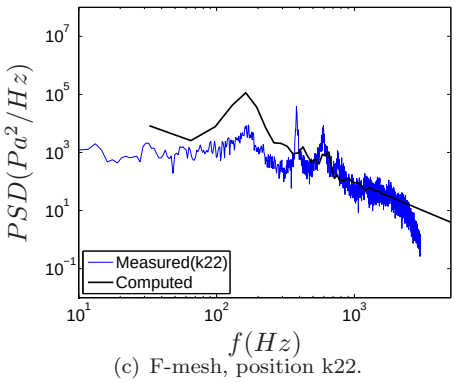

(c) F-mesh, position k22.

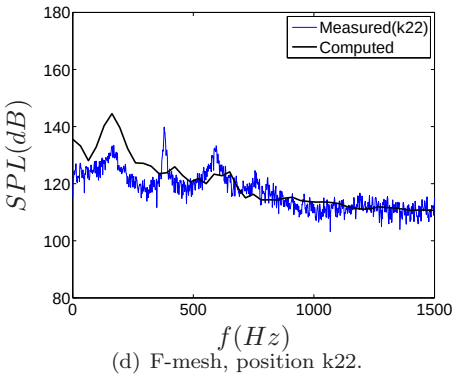

(d) F-mesh, position k22.

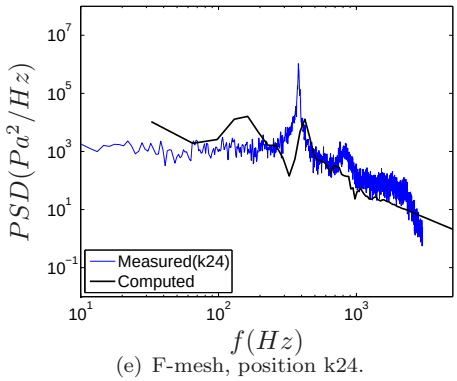

(e) F-mesh, position k24.

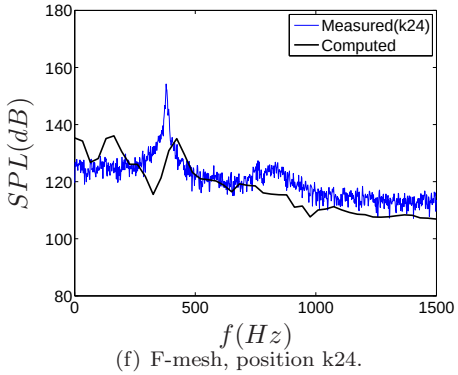

(f) F-mesh, position k24.

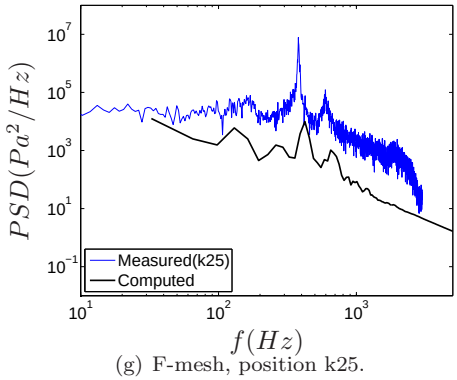

(g) F-mesh, position k25.

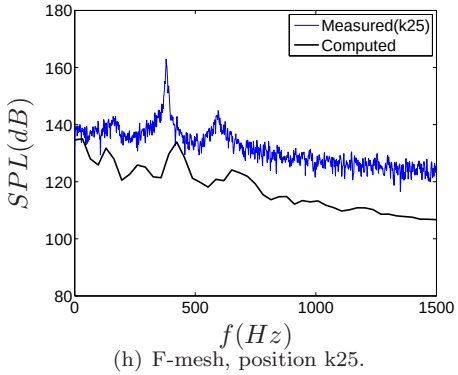

(h) F-mesh, position k25.

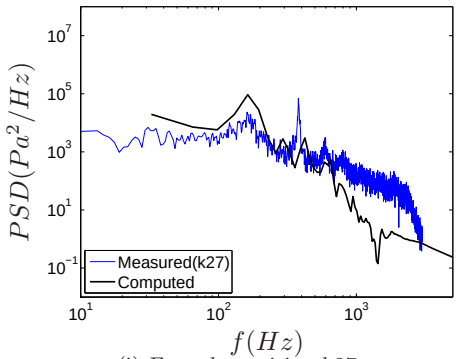

(i) F-mesh, position k27.

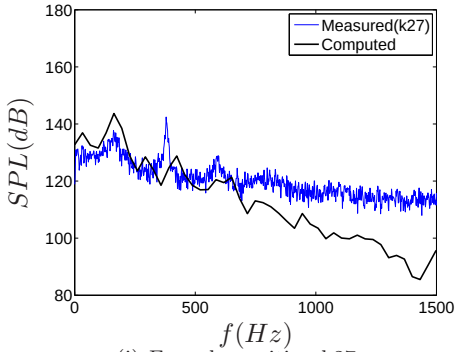

(j) F-mesh, position k27.

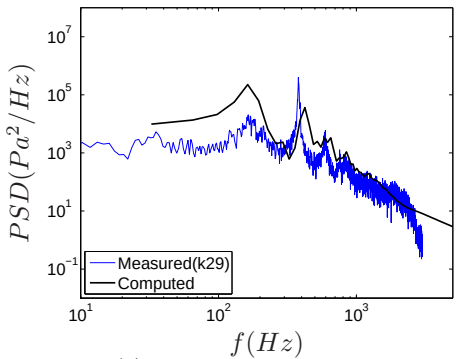

(k) F-mesh, position k29.

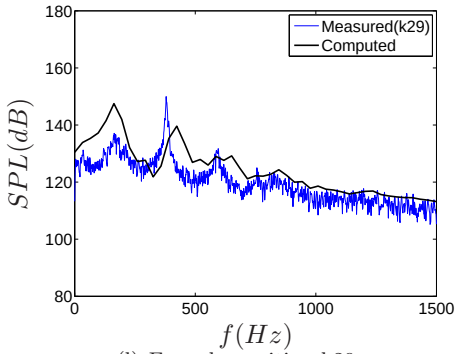

(l) F-mesh, position k29.

Figure 3.11: F-mesh: computed PSD of pressure fluctuations and SPL at positions, k20, k22, k24, k25, k27 and k29 on the surface of cavity floor.

In Figure 3.12, the computed PSD and SPL at positions k17 and k18 on the cavity rear wall are presented. It is shown that the prediction for the first mode agrees fairly well with the measured data in terms of both the frequency and the magnitude. Similar to that at other positions, however, the predicted frequency for the second mode is over-estimated with a lower tonal peak.

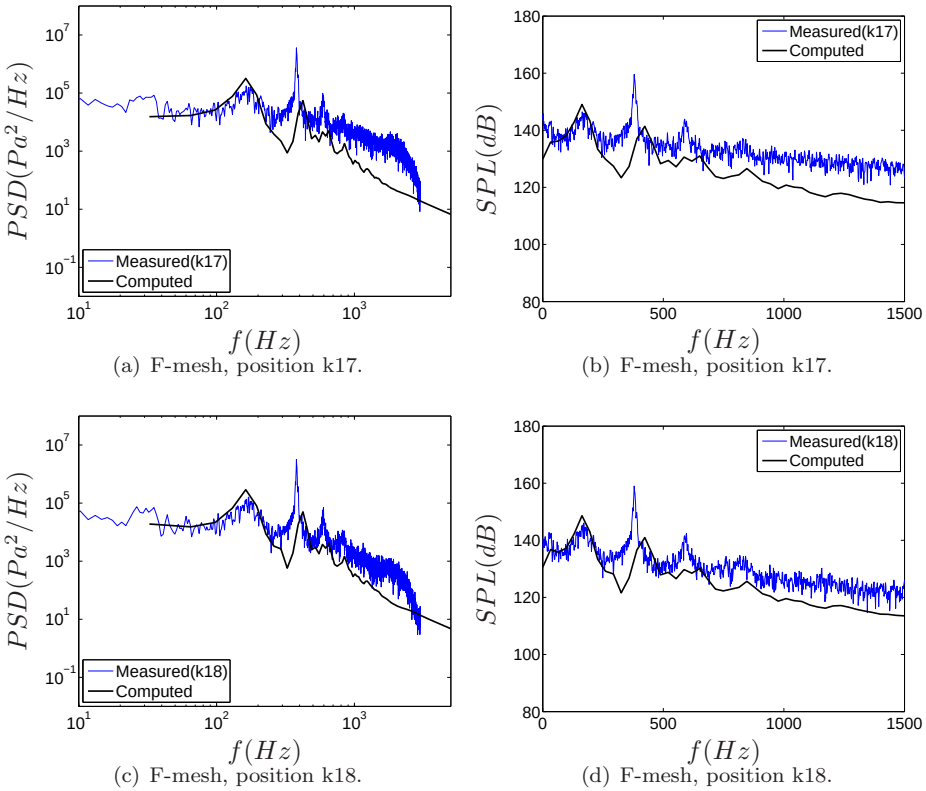

(a) F-mesh, position k17.
(b) F-mesh, position k17.
(c) F-mesh, position k18.
(d) F-mesh, position k18.

Figure 3.12: F-Mesh: computed PSD of pressure fluctuations and SPL at positions k17 and k18 on the rear-wall surface of the cavity.

3.2 Cross comparison of computations with different meshes

One of the main purposes with the present 2D computations is to investigate the effect of the mesh resolution. From the C-mesh to the M-mesh, the grid in the cavity is refined in the streamwise x-direction but not in the vertical y-direction. With the same computational domain, the M-mesh has refined appreciably the block above the cavity in both the streamwise and vertical directions. With the NM-mesh and the F-mesh, the computational domain is reduced in the vertical direction (from $L_y = 17D$ to $L_y = 7.5D$). This has resulted in a better grid resolution in the region above the cavity and for the incoming boundary layer without drastic increase of grid nodes. It should be recognized here that the reduced computational domain may trigger inappropriateness in the specification of boundary conditions, particularly on the upper boundary, where a symmetric boundary condition has been assumed. The number of grid nodes in the NM-mesh is similar to that in the C-mesh, but with a somewhat improved resolution in the incoming boundary layer and in the shear layer over the cavity opening. With F-mesh the grid resolution is overall improved and the meshing is much less stretched with a moderate cell aspect ratio.

A cross comparison is made below for the results computed with different meshes. In Figure 3.13 the time series of pressure fluctuations is compared with the experimental measurements at, respectively, six positions on the cavity floor (k20, k22, k24, k25, k27 and k29) and two positions on the cavity rear wall (k17 and k18). The experiment shows a general tendency of increasing pressure fluctuations from the front wall to the rear wall along the cavity floor. Note that the time series with the NM-mesh is not recorded at k22, k27 and k18. Both the C-mesh and the M-mesh have significantly over-predicted the fluctuation at all positions. With the NM-mesh, the over-prediction has been diminished but not at position k20 near the left-hand-side corner below the cavity front wall. When the mesh is further refined with the F-mesh, the discrepancy between the predicted level of the pressure fluctuation and the measured one has been further reduced, though $p'(t)$ is significantly underestimated at position k25.

The acoustic tones that radiated from the cavity correspond to characteristic pressure patterns (standing waves or acoustic mode shapes) in the cavity. In Figures 3.14 and 3.15, a cross comparison due to different grid resolutions is made for PSD and SPL respectively at locations k20, k22, k24, k25, k27, k29, k17 and k18. As compared with the experiment, additional unphysical modes have been produced with the C-mesh and NM-mesh, as well as with the M-mesh from which the additional modes are less sensible though. The C-mesh has generally over-estimated the tonal magnitudes. The first mode has been predicted by the C-mesh at a lower frequency than the measured $f_1 = 180Hz$, while the third predicted mode corresponds to the second mode from the experiment at an approximately similar frequency. The measured third tonal mode matches approximately the predicted fifth mode that has a slightly larger frequency. Refining the mesh to the M-mesh, the additionally generated tones persists but with reduced magnitudes. The predicted third mode (corresponding to the measured second mode in terms of frequency) becomes less distinguished than that with the C-mesh. The NM-mesh is able to give improved prediction to the frequency for the first mode but fails to regenerate other tonal modes. The F-mesh has enabled an overall improvement in prediction of PSD and SPL, particularly for the first mode in terms of both the magnitude and frequency. The unphysical modes have been diminished with the F-mesh. Not very sensible though, the F-mesh produces also the second mode but with a somewhat larger frequency than the measured one.

In Figure 3.16, a comparison is made for the time-averaged sound pressure level, $\overline{SPL}$, see Eq. (3.4), computed with different meshes along the cavity floor. As already demonstrated in the presentation of PSD and SPL, the C-mesh, M-mesh and NM-mesh have in general over-predicted the first mode. This has consequently made the level of $\overline{SPL}$ overestimated. The result is similar to the 2D prediction by Ashworth [12] using the CFX code on the same computational domain gridded with the M-mesh. When the NM-mesh is used, $\overline{SPL}$ at positions k24 and k25 is under-predicted as compared with the measurement. The F-mesh gives the closest prediction to the experiment, which over-estimates, nonetheless, the rms of $p'(t)$ at position near the the front wall (k20 and k22) and under-predicts it at positions from the mid-section of the floor to the rear wall (from k24 to k29). In contrast to the measured tendency, which presents an increased $\overline{SPL}$ from k22 to k24 and a reduced $\overline{SPL}$ from k24 to k26, the predicted variation of $\overline{SPL}$ along the cavity floor shows an opposite profile with all mashes. This may imply that the predicted pressure pattern in the mid-section of the cavity floor does not match the characteristic pattern as measured in the experiment.

It should be noted, in addition, that the pressure fluctuation as shown in Figure 3.13 presents a clear cyclical pressure oscillation. Similar periodic oscillations have also been identified in other 2D computations [8, 19]. An

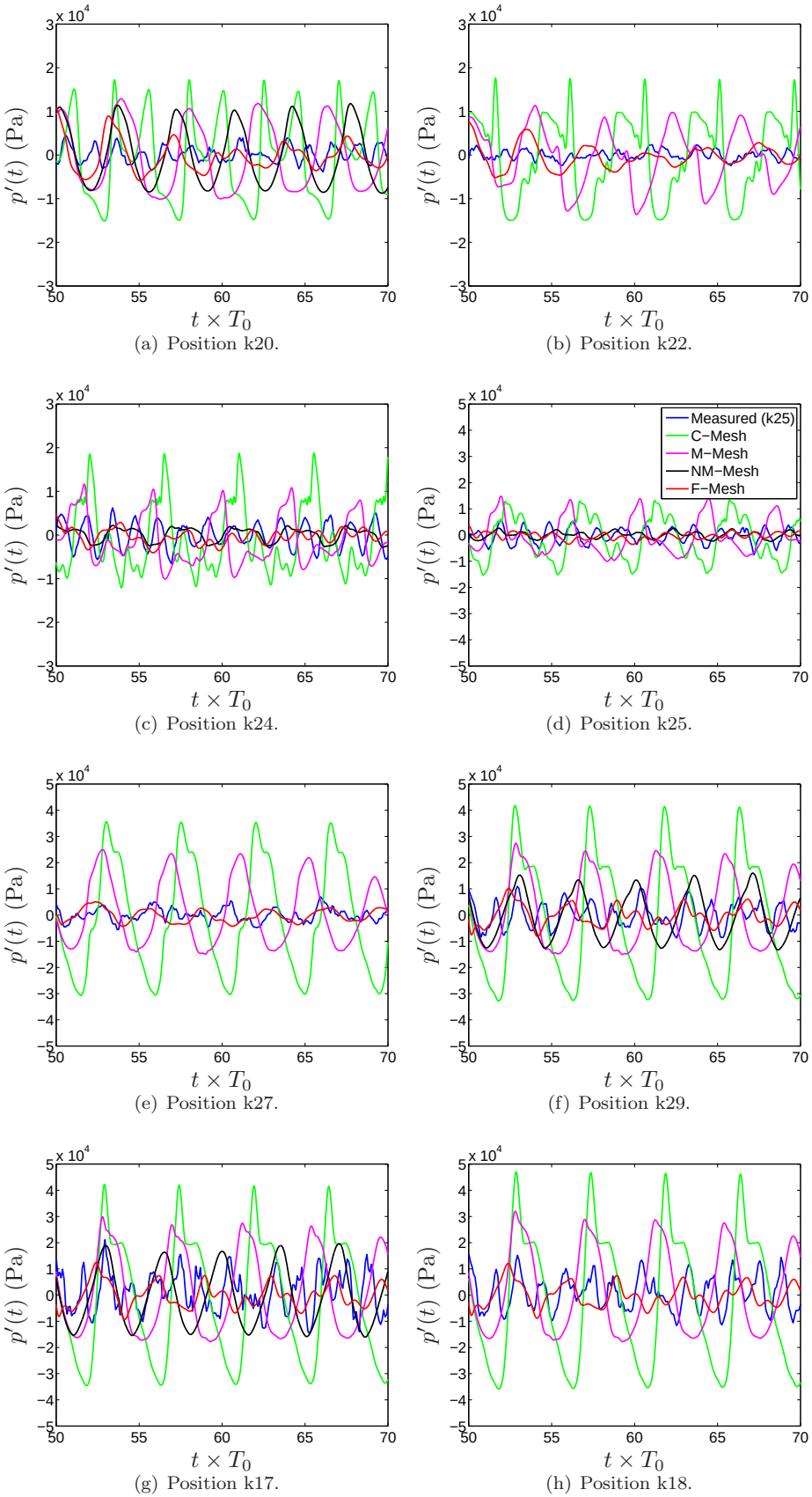

(a) Position k20. (b) Position k22.

(c) Position k24. (d) Position k25.

(e) Position k27. (f) Position k29.

(g) Position k17. (h) Position k18.

Figure 3.13: Comparison of pressure fluctuations computed at positions, k20, k22, k24, k25, k27, k29 k17 and k18.

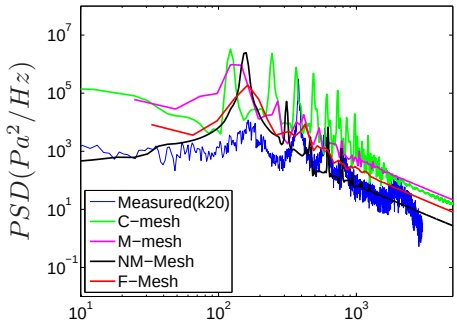

(a) Position k20.

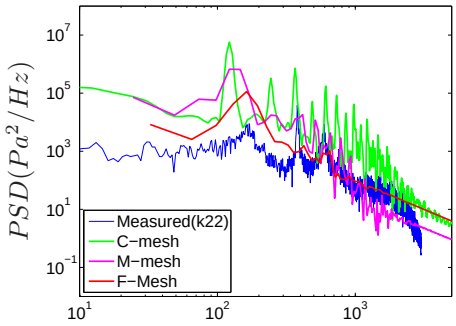

(b) Position k22.

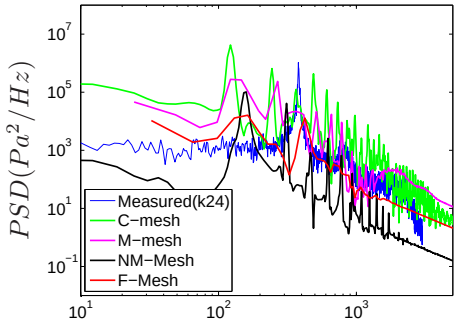

(c) Position k24.

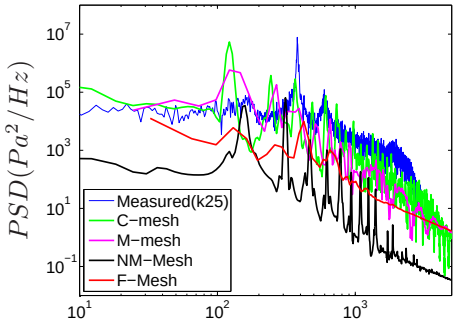

(d) Position k25.

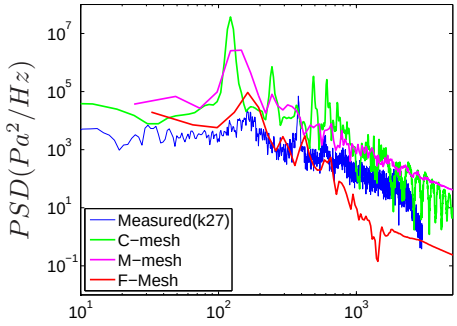

(e) Position k27.

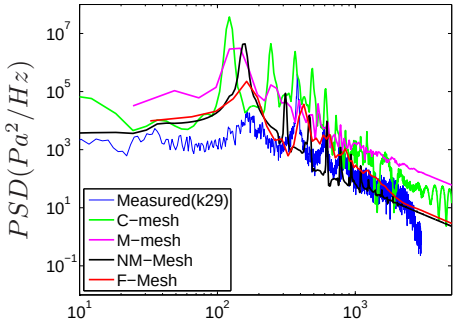

(f) Position k29.

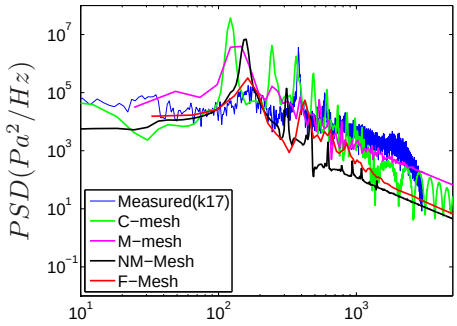

(g) Position k17.

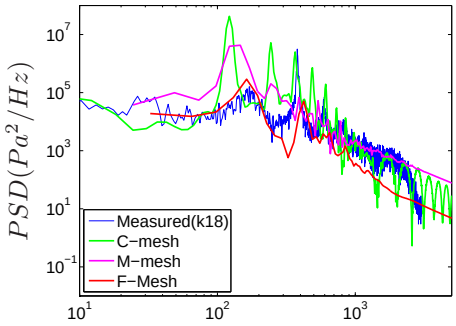

(h) Position k18.

Figure 3.14: Comparison of pressure fluctuations computed at positions, k20, k22, k24, k25, k27, k29 k17 and k18.

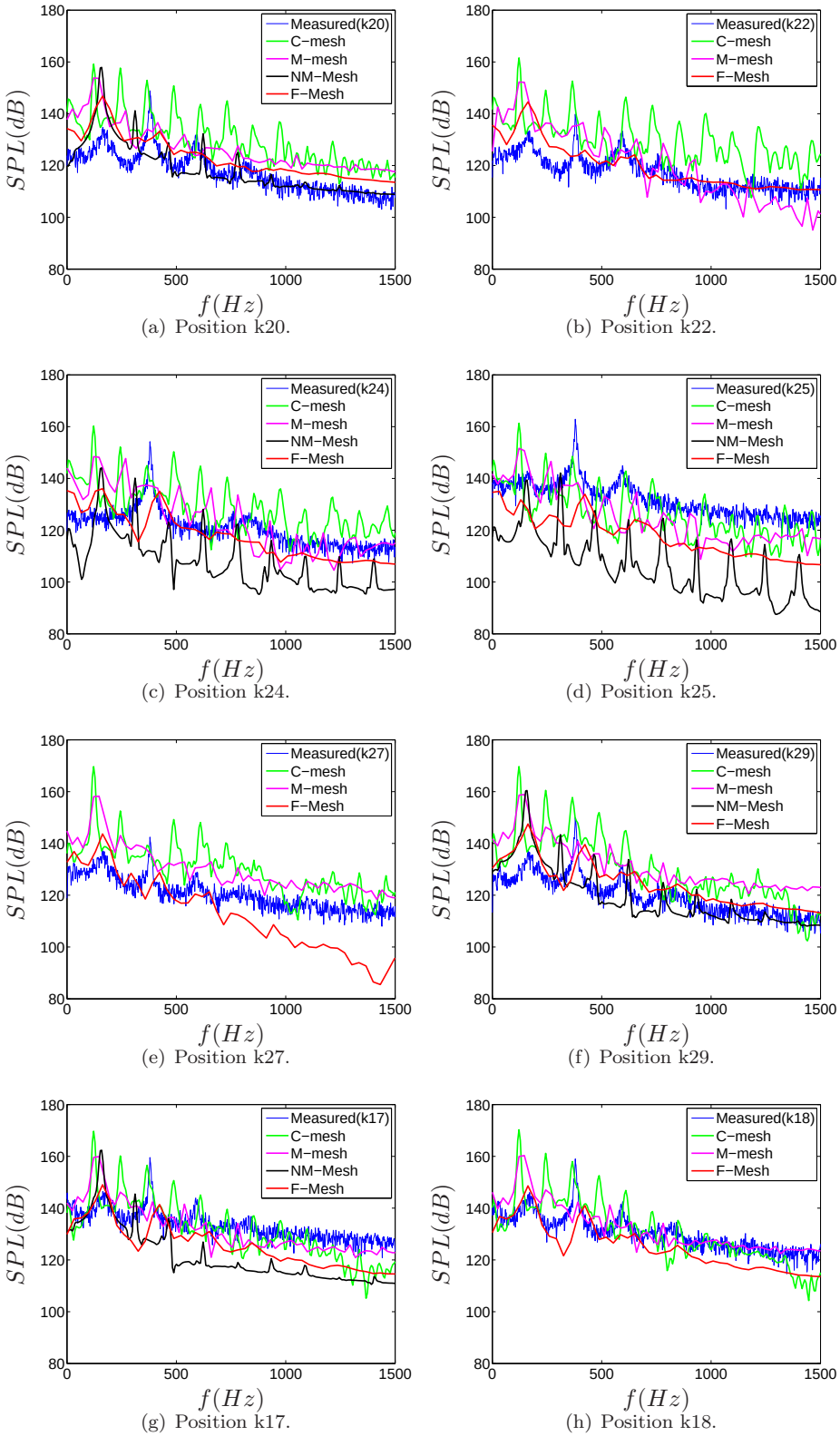

(a) Position k20. (b) Position k22.

(c) Position k24. (d) Position k25.

(e) Position k27. (f) Position k29.

(g) Position k17. (h) Position k18.

Figure 3.15: Comparison of pressure fluctuations computed at positions, k20, k22, k24, k25, k27, k29 k17 and k18.

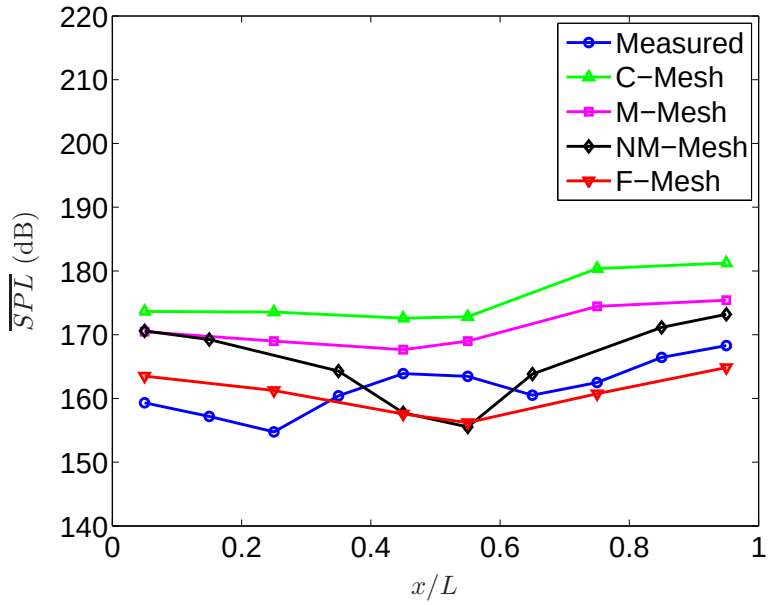

Figure 3.16: Comparison of $\overline{SPL}$ computed with different meshes.

oscillation cycle can be defined from the pressure time series (Figure 3.13) by taking the time interval between two pressure peaks. The dominant frequency of oscillation can then be obtained by taking directly the reciprocal of the time interval (time period). This estimated time cycle and the corresponding frequency are given in table 3.1. The identified frequency from the cyclic pressure oscillation corresponds to the frequency of the predicted first mode.

Mesh	C-mesh	M-mesh	NM-mesh	F-mesh
Dominant frequency (Hz)	124	130	164	176
Time period	$4.42T_0$	$4.21T_0$	$3.34T_0$	$3.11T_0$

Table 3.1: Frequencies identified from the cyclic pressure oscillation with different meshes. Note that the measured tonal frequency for the first model is $f_1 \approx 180Hz$.

It is noted here that the cyclic pressure oscillation occurs when the flow is fully developed. The frequency is often rather regular, but the magnitude may slightly differ from time to time. This is particularly the case with the M-mesh and the F-mesh. With the C-mesh and NM-mesh, the oscillation shows a very regular cycle in terms of both the time period and the fluctuating magnitude. Figure 3.17 illustrates a typical cycle of the flow field obtained with the C-mesh, where the flow field advances at a time step of $\Delta t = 1.1T_0$ starting from time t_0. It is clearly shown that the unsteady flow pattern has a cycle of about $4.4T_0$, which corresponds approximately to the frequency of $f_1 = 124Hz$, as identified in Table 3.1

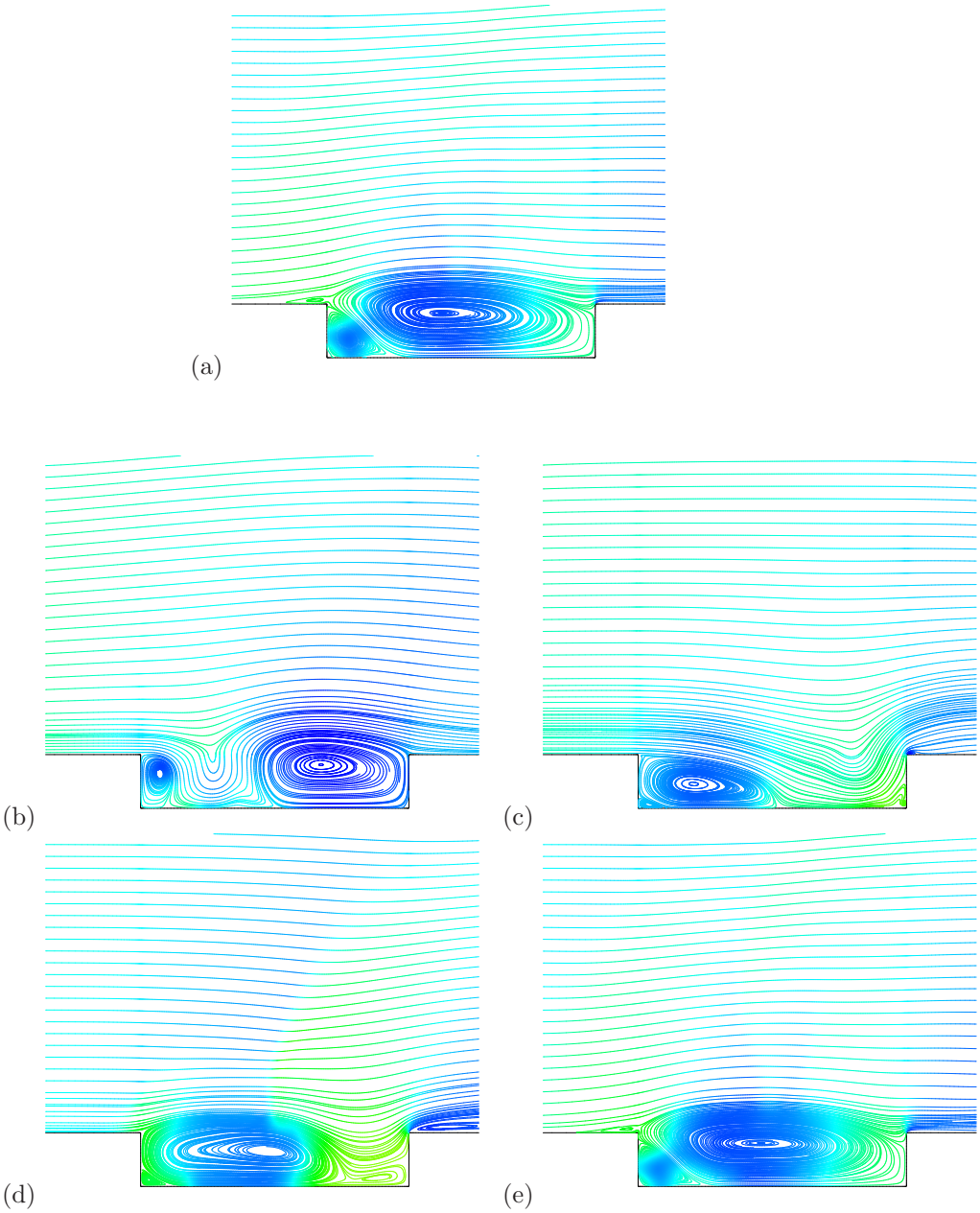

Figure 3.17: Computed unsteady flow fields at different times. The time-scale T_0 used for normalization is $T_0 = L/U_\infty$. (a) at $t = t_0$; (b) at $t = t_0 + 1.1T_0$; (c) at $t = t_0 + 2.2T_0$; (d) at $t = t_0 + 3.3T_0$; e) at $t = t_0 + 4.4T_0$.

4 Summary

This memorandum summarizes the results of some 2D baseline computations for a subsonic cavity flow, which simulates the configuration of a weapon bay at $M_\infty = 0.85$ during a store-release operation. The calculations are based on unsteady RANS simulations using the Spalart-Allmaras model to account for the turbulence effect. The FOI in-house structured, multi-block code EURANUS has been used for all the computations presented. The emphasis has been placed on the effect of grid resolution, for which four groups of meshes have been involved. Based on the results, the pressure fluctuations, recorded in a number of time series at positions along the cavity floor and on the cavity rear wall, respectively, have been analyzed in terms of the power spectral density (PSD) and the sound pressure level (SPL). The results are compared with available experimental data.

The C-mesh is a baseline coarse mesh. The medium mesh, M-mesh is gridded on the same computational domain as with the C-mesh and is moderately refined both in the cavity and in the domain above the cavity, mainly in the streamwise $x-$direction. The computational domain meshed with the non-matching mesh (NM-mesh) and the fine mesh (F-mesh) has a reduced size in the vertical direction. The NM-mesh is divided into two blocks, consisting of the cavity part and the region above the cavity, respectively. The two blocks have a common interface gridded with non-matching nodes, where the block containing the cavity has a finer streamwise resolution than another block. As compared with the C-mesh, the NM-mesh has a similar number of grid nodes meshed in the cavity and in total. Nevertheless, due to the reduced domain size in L_y, the NM-mesh has significantly refined the mesh in the vertical direction for the block above the cavity. With the F-mesh, effort has been made to generate an overall less stretched mesh with significant grid refinement in the cavity, as well as in the incoming boundary layer and in the shear layer across the cavity opening.

In the analysis of PSD and SPL, the computation generates predictions similar to those obtained in other 2D simulations for cavity flows in the literature. It is shown that the C-mesh and NM-mesh produce additional unphysical tonal modes, as compared with the experimental measurements. The first pressure mode predicted with the C-mesh has a frequency of $124Hz$ compared to the measured $180Hz$. The magnitudes of PSD and SPL have been in general over-predicted. It is noticed that the predicted third mode with the C-mesh corresponds to the measured second mode, but at a somewhat lower frequency than the measured $f_2 = 390Hz$. The M-mesh is able to bring down to some extent the over-predicted tonal magnitude. It predicts the first tonal mode at $f_1 = 130Hz$. With the NM-mesh, which gives a finer vertical resolution than both the C-mesh and the M-mesh in the shear layer over the cavity opening, the predicted magnitudes of PSD and SPL have been further reduced, and are even under-estimated in comparison with the experiment in the mid-range of $0.45 \leq x/L \leq 0.65$ on the cavity floor. The prediction has also produced additional unphysical tones, but the first mode is better captured in terms

of the tonal frequency, giving $f_1 = 164Hz$, whilst the magnitude is generally over-estimated. This seems to imply that the first mode is closely related to the resolution of the shear layer. The overall refined F-mesh is able to smooth the additional unphysical tonal modes with two distinguishable modes being persisted, namely, the first and the second mode. The predicted first mode has a frequency of $f_1 = 176Hz$, which is close to the measured $f_1 = 180Hz$. The magnitude of this mode is generally over-estimated on the cavity floor (but not for k25 at $x/L = 0.55$), where it is under-predicted), but much better than the prediction with other meshes. On the cavity rear wall (positions k17 and k18), the magnitude has also been predicted fairly well. The predicted second mode is less sensible with an under-estimated magnitude and a larger frequency than measured in the experiment. The comparison of PSD and SPL predicted with different meshes highlights the importance of mesh resolution in the incoming boundary layer and in the subsequent shear layer, as well as in the cavity. An insufficient mesh resolution may generate additional tonal modes and under-predicts the tonal frequency for the first mode, while over-estimating its magnitude. A refined mesh is able to diminish these unphysical patterns and improve the prediction for the first and second modes in terms of both the tonal frequency and magnitude. It seems that the first two tonal modes for the case considered may be resolved with a certain accuracy using URANS modelling with an appropriate grid refinement.

In addition, the 2D computation shows that the flow field exhibits cyclic pressure oscillations with a time period between $3T_0$ and $4.5T_0$ upon the mesh resolution used. It is shown that the instability of the shear layer after the upstream incoming boundary layer dominates the flow pattern in the cavity and, consequently, characterizes the pressure oscillation in the cavity and thus on the cavity wall surface. Obviously, an appropriate resolution of this shear layer and the consequent flow phenomena in the cavity is the key to reach accurate predictions of the pressure patterns and related sound resonance.

It should be recognized that the the number of sampling data in the computation with the F-mesh is relatively small, which was terminated due to the CFD code was switched from the structured EURANUS to the unstructured EDGE code. In addition, the reduced computational domain as used in the NM-mesh and F-mesh simulations may probably introduce some errors with the symmetric condition imposed on the top boundary of the computational domain. Moreover, it is noted that the 2D computation has ruled out any three-dimensional effects, which practically exist in the experimental measurement. The door-on case may partly regulate the flow similar to a 2D type in the mid-section of the spanwise direction, but the influence of the spanwise cavity side-walls may not be negligible. Nonetheless, the implications gained from these 2D computations are valuable for the subsequent 3D computations. Indeed, a 3D computation for the same problem has shown significantly improved predictions using the same RANS model, which will be presented in a separate report.

Bibliography

[1] A. Roshko. Some measurements of flows in a rectangular cutout. NACA TN 3488, 1955.

[2] T. Colonius. An overview of simulation, modeling, and active control of flow/acoustic resonance in open cavities. AIAA Paper 2001-0076, 2001.

[3] V. Sarohia. *Experimental and analytical investigation of oscillations in flows over cavities*. PhD thesis, California Institute of Technology, USA, 1975.

[4] M. Gharib and A. Roshko. The effect of flow oscillations on cavity drag. *Journal of Fluid Mechanics*, 177:501–531, 1987.

[5] C. W. Rowley, T. Colonius, and A. J. Basu. On self-sustained oscillations in two-dimensional compressible flow over rectangular cavities. *Journal of Fluid Mechanics*, 455:315–346, 2002.

[6] J. E. Rossiter. Wind tunnel experiments on the flow over rectangular cavities at subsonic and transonic speeds. Rep. Mem. 3438, Aeronautical Research Council, 1964.

[7] S. Srinivasan and O. Baysal. Navier-Stokes calculations of transonic flow past cavities. *Journal of Fluid Engineering*, 113:369–376, 1991.

[8] C.-J. Tam, P. D. Orkwis, and P. J. Disimile. Algebraic turbulence model simulations of supersonic open-cavity flow physics. *AIAA Journal*, 34:2255–2260, 1996.

[9] S. T. Shih and P. J. Morris. Parallel computational aeroacoustic simulation of turbulent subsonic cavity flows. AIAA Paper 2000-1914, 2000.

[10] M. J. Stanek, G. Raman, V. Kibens, J. A. Ross, J. Odedra, and J. W. Peto. Control of cavity resonance through very high frequency forcing. AIAA Paper 2000-1905, 2000.

[11] M. J. Stanek, G. Raman, V. Kibens, J. A. Ross, J. Odedra, and J. W. Peto. Supression of cavity resonance using high frequency forceing- the characteristic signature of effective devices. AIAA Paper 2001-2128, 2001.

[12] R. M. Ashworth. TurMMAC weapon bay application chanllenge- final analysis. Rept. TFD/94/10, QinetiQ/FST/AVS/TR046679, 2004.

[13] A. Rizzi, P. Eliasson, I. Lindblad, C. Hirsch, C. Lacor, and J. Haeuser. The engineering of multiblock/multigrid software for Navier-Stokes flows on structured meshes. *Computers & Fluids*, 22:341–367, 1993.

[14] FFA. EURANUS v5.2 users guide. FFA TN, Flygtekniska Försökanstalten, Stockholm, 1998.

[15] P. R. Spalart and S. R. Allmaras. A one-equation turbulence model for aerodynamic flows. AIAA Paper 92-0439, Reno, 1992.

[16] D. A. Peshkin. TurMMAC application challenge test case specification: M219 cavity. QinetiQ/FST/CAT/WP020905, 2002.

[17] D.C. Wilcox. Reassessment of the scale-determining equation for advanced turbulence models. *AIAA J.*, 26(11):1299–1310, 1988.

[18] M. B. Tracy, E. B. Plentovich, and J. Chu. Measurements of fluctuating pressure in a rectangular cavity in transonic flow at high Reynolds numbers. NASA Tech. Memorandum 4363, 1992.

[19] P. D. Orkwis, B. Sekar, S. Chakravarthy, and O. Peroomian. Comparison of three Navier-Stokes equation solvers for supersonic open cavity simulation. *AIAA Journal*, 36:865–867, 1998.